

# Galactic foreground contributions to the *WMAP5* maps

N. Macellari,<sup>1</sup> E. Pierpaoli,<sup>1</sup> C. Dickinson,<sup>2</sup> & J. E. Vaillancourt<sup>3</sup>

<sup>1</sup> *University of Southern California, Los Angeles, CA 90089-0484, U.S.A.*

(*macellar@usc.edu, pierpaol@usc.edu*)

<sup>2</sup> *Jodrell Bank Centre for Astrophysics, Alan Turing Building, School of Physics & Astronomy, University of Manchester, Oxford Road, Manchester, M13 9PL, U.K.*

(*Clive.Dickinson@manchester.ac.uk*)

<sup>3</sup> *Division of Physics, Mathematics, & Astronomy, California Institute of Technology, 1200 E. California Blvd., Pasadena, CA 91125, U.S.A.*

*Current address: Stratospheric Observatory for Infrared Astronomy, Universities Space Research Association, NASA Ames Research Center, Moffett Field, CA (jvaillancourt@sofia.usra.edu)*

Accepted ???. Received ???; in original form ???

## ABSTRACT

We compute the cross correlation of the intensity and polarisation from the 5-year *WMAP* data in different sky-regions with respect to template maps for synchrotron, dust, and free-free emission. We derive the frequency dependence and polarisation fraction for all three components in 48 different sky regions of HEALPix ( $N_{\text{side}} = 2$ ) pixelisation. The anomalous emission associated with dust is clearly detected in intensity over the entire sky at the K (23 GHz) and Ka (33 GHz) *WMAP* bands, and is found to be the dominant foreground at low Galactic latitude, between  $b = -40^\circ$  and  $b = +10^\circ$ . The synchrotron spectral index obtained from the K and Ka *WMAP* bands from an all-sky analysis is  $\beta = -3.32 \pm 0.12$  for intensity and  $\beta = -3.01 \pm 0.03$  for the polarised intensity.

The polarisation fraction of the synchrotron is constant in frequency and increases with latitude from  $\approx 5\%$  near the Galactic plane up to  $\approx 40\%$  in some regions at high latitude; the average value for  $|b| < 20^\circ$  is  $8.6 \pm 1.7$  (stat)  $\pm 0.5$  (sys) % while for  $|b| > 20^\circ$  it is  $19.3 \pm 0.8$  (stat)  $\pm 0.5$  (sys) %. Anomalous dust and free-free emission appear to be relatively unpolarised. Monte carlo simulations showed that there were biases of the method due to cross-talk between the components, at up to  $\approx 5\%$  in any given pixel, and  $\approx 1.5\%$  on average, when the true polarisation fraction is low (a few per cent or less). Nevertheless, the average polarisation fraction of dust-correlated emission at K-band is  $3.2 \pm 0.9$  (stat)  $\pm 1.5$  (sys) % or less than  $5\%$  at 95 % confidence. When comparing real data with simulations, 8 regions show a detected polarisation above the 99th percentile of the distribution from simulations with no input foreground polarisation, 6 of which are detected at above  $2\sigma$  and display polarisation fractions between  $2.6\%$  and  $7.2\%$ , except for one anomalous region, which has  $32 \pm 12\%$ . The dust polarisation values are consistent with the expectation from spinning-dust emission, but polarised dust emission from magnetic-dipole radiation cannot be ruled out. Free-free emission was found to be unpolarised with an upper limit of  $3.4\%$  at 95 % confidence.

**Key words:** ISM: general – Galaxy: general – cosmology: diffuse radiation – cosmology: cosmic microwave background – radio continuum: ISM

## 1 INTRODUCTION

During the last few years, great advances have been made in measuring the Cosmic Microwave Background (CMB) anisotropies. More advances are expected from the *Planck* mission that will provide all-sky temperature and polarisation CMB measurements with high accuracy and unprecedented frequency coverage. As CMB experiments reach higher sensitivity, it becomes necessary to better understand and remove the contribution from competing Galactic and extragalactic astrophysical signals in the same frequency bands. It is well known that the emission of these foregrounds rivals the temperature signal over a significant fraction of the sky and dominates the polarisation signal over most of the sky (Kogut

et al. 2007). As the temperature power spectrum has already been measured with great precision (e.g., *WMAP5*, Nolta et al. 2009; ACBAR, Reichardt et al. 2009; Boomerang, Jones et al. 2006; CBI, Sievers et al. 2009; VSA, Dickinson et al. 2004; QUaD, Pryke et al. 2009), most observations are now concentrating on polarisation measurements (e.g., BICEP, Chiang et al. 2009; QUaD, Brown et al. 2009). For the study of polarisation anisotropies however, foregrounds may be the limiting factor, as the primordial signal is much weaker than intensity while the foregrounds are not well characterised at the relevant frequencies at this time. For this reason, suitable component separation techniques have been developed and are being applied to current data (Kogut et al. 2007; Eriksen et

al. 2008; Gold et al. 2009; Dunkley et al. 2009; Delabrouille & Cardoso 2009), in preparation for *Planck* data, and possible future missions (Leach et al. 2008; Betoule et al. 2009). In some instances such techniques rely on prior information acquired on the emission of a specific foreground, for which a prior characterisation is necessary. Moreover, the study of foregrounds in the microwave band is of astrophysical interest on its own, as it can be informative about physical phenomena occurring in our Galaxy and in others.

Foregrounds are either Galactic or extragalactic in nature. In this paper we are interested in the Galactic emission, which dominates over extragalactic emission at intermediate to large scales ( $\gtrsim 1^\circ$ ). The Galactic emission has three main components: dust, synchrotron, and free-free, of which only dust and synchrotron are expected to show significant polarisation. In contrast with extragalactic emission, we do not expect the Galactic foreground to be isotropic. For this reason, Galactic foregrounds need a characterisation that is both scale dependent and position dependent.

The most common methods for extracting foreground information from CMB data involve fitting a given theoretical model to the data. These fitting procedures typically assume that a specific foreground follows a power-law in frequency and is characterised by a given polarisation fraction and a (fixed) angle. For instance, this is the approach of the *WMAP* teams (Kogut et al. (2007) for the *WMAP* 3-year and Gold et al. (2009) for the *WMAP* 5-year data).

By so doing, however, the diverse behaviour of different foregrounds in different regions of the sky may be neglected. For instance, a spinning-dust contribution may not have a power-law frequency dependence, and may make different contributions in different areas of the sky. A variety of dust grains may populate different areas of our galaxy, and have different contributions to the intensity and polarisation signal at the observed frequencies. The synchrotron emission clearly depends on the energy spectrum of electrons in a given region, while the polarisation signal may be affected by depolarisation effects which are more severe in denser or less uniform regions.

In this paper, we aim to characterise the contribution of the three Galactic components in the microwave band in temperature and polarisation by studying the *WMAP5* data (Nolta et al. 2009; Hinshaw et al. 2009), including their frequency and spatial dependencies. To achieve this goal we develop a foreground analysis that assumes no frequency model and only relies on a morphological characterisation of foregrounds as derived at non-CMB frequencies. Specifically, we use a cross-correlation (C-C) analysis with standard foreground templates. Such an analysis method has been widely used by other authors studying CMB intensity data (e.g., de Olivera-Costa et al. 1999, 2002; Banday et al. 2003; Bennett et al. 2003; Davies et al. 2006), but has not been applied to polarisation data. An advantage of using such a method is the possibility of detecting particular emission processes associated with one of the three foreground templates even if its frequency and/or polarisation characteristics are unknown. For example, this may be true in the case of a spinning-dust component.

A possible limitation of the C-C method is that it allows characterisation of only foreground components whose spatial distribution is well traced by the templates. These templates were derived at very different frequencies than the CMB measurements, and may not fully represent the morphology of a particular component in the range of frequencies at hand. Most analyses of *WMAP5* polarisation data are based on modelling the various emission components in the *Q* and *U* maps; here we will perform our analysis in the polarisation intensity *P*. This choice avoids the problem of modelling the Galactic magnetic field to compute the polarisation angle, or

assuming a specific polarisation angle as a function of position for each component. Under the hypothesis that all components have the same polarisation angle (even if possibly a different polarisation intensity), the method used in analysing the temperature maps can be readily extended to the polarisation maps. Although a more general approach may be sought, as both dust grains' orientation and synchrotron emission are dictated by the direction of the magnetic field, this assumption may not be unreasonable.

Section 2 describes the *WMAP* data used in this work and the choices made about spatial resolution and masking, while Section 3 gives an introduction to the various sources of foreground emission and the spatial templates that will be used to trace each component. The cross-correlation analysis technique and the computation of uncertainties are derived in Section 4. The results of the analysis in both temperature and polarisation are presented in Section 5, along with separate discussions for each of the 3 emission components. The main conclusions are summarised in Section 6.

## 2 WMAP DATA

We use the *WMAP* 5-year data (Hinshaw et al. 2009), consisting of 5 full-sky maps at frequencies of 22.8 GHz (K-band), 33.0 GHz (Ka-band), 40.7 GHz (Q-band), 60.8 GHz (V-band), and 93.5 GHz (W-band), as provided by the LAMBDA website<sup>1</sup>. These maps are provided in HEALPix<sup>2</sup> format at a resolution of  $N_{\text{side}} = 512$  (number of pixels on the sphere =  $12 \times N_{\text{side}}^2$ ). The maps are then downgraded to a HEALPix resolution of  $N_{\text{side}} = 32$ , using the `ud_grade`<sup>3</sup> HEALPix routine, to give a total of 12,288 pixels. We chose this resolution as a compromise between obtaining a reasonable signal-to-noise ratio and having small enough pixels to keep the information about foreground variations needed in the C-C analysis; with  $N_{\text{side}} = 16$  the resolution is becoming too coarse. Larger pixels are also likely to invalidate the assumption of a constant polarisation fraction. Parallel transport of polarisation vectors on the sphere is not considered in the averaging since the effect is at the  $10^{-4}$  level or lower.

We convert the data from thermodynamic temperature to brightness (antenna) temperature using the conversion:

$$T_A = \frac{x^2 e^x}{(e^x - 1)^2} T_{\text{CMB}} \quad (1)$$

where  $x \equiv (h\nu)/(kT_0)$  and  $T_0$  is the CMB temperature of  $2^\circ 725$  K (Mather et al. 1999); this corresponds to a correction of 1% at K-band and 25% at W-band.

We apply the *WMAP* team mask KQ85 (Gold et al. 2009) to the *WMAP* maps, in order to avoid the Galactic plane and bright point sources. The mask is provided in a  $N_{\text{side}} = 512$  HEALPix resolution, so we downgrade it to our working resolution ( $N_{\text{side}} = 32$ ) and consider in the analysis only the coarse pixels that are completely outside of the  $N_{\text{side}} = 512$  masked region. This procedure reduces to 8099 the number of data pixels (66% of the sky) used in the analysis.

In the polarisation analysis we compute the total polarisation as  $P = \sqrt{Q^2 + U^2}$ . The mask and the resolution chosen are the same as the intensity analysis. This allows direct comparison of the C-C coefficients fit for the temperature and polarisation data and calculation of the fractional polarisation at the same sky positions.

<sup>1</sup> <http://lambda.gsfc.nasa.gov/>

<sup>2</sup> <http://www.eso.org/science/healpix/> (Górski et al. 2005)

<sup>3</sup> Simple averaging is used, rather than a noise-weighted average.

### 3 GALACTIC COMPONENTS EMISSION AND TEMPLATES

#### 3.1 Synchrotron

Synchrotron emission arises from accelerating cosmic ray electrons spiralling in the Galactic magnetic field. The emission depends on the energy spectrum of the electrons and on the intensity of the magnetic field, which results in significant spatial variations in the spectral index on the sky. The synchrotron spectrum is approximated by a power law  $T \sim \nu^\beta$ , typically with  $\beta \approx -2.7$  at radio wavelengths, steepening to  $\beta \approx -3.0$  at *WMAP* frequencies and with typical spatial variations of  $\pm 0.2$ . Moreover, it is known that a pure synchrotron spectrum steepens with frequency due to the effects of spectral ageing, although in reality, a flattening of the spectrum can occur due to the presence of multiple components (e.g., Kogut et al. 2007).

Most of the information we have for synchrotron emission comes from low frequency radio surveys, where synchrotron dominates the sky. In particular, large-area radio surveys at 408 MHz (Haslam et al. 1981, 1982), 1420 MHz (Reich & Reich 1986) and 2.3 GHz (Jonas et al. 1998) give us a clear picture of the synchrotron component and these have been used extensively for foreground subtraction and previous cross-correlation studies. The drawbacks of using such templates are i) there is a large extrapolation in frequency from  $\sim 1$  GHz to *WMAP* frequencies that is likely to result in some distortion of the morphology, ii) baseline (offset) issues result in striping in the maps, and iii) discrete extragalactic sources contaminate the diffuse emission. Several efforts have been made to reduce the effects of striping and source contamination (e.g., Davies et al. 1996; Platania et al. 2003) including the NCSA version of the Haslam et al. 408 MHz map, available at the LAMBDA website. We use this as our template for synchrotron emission.

Synchrotron emission is, by nature, highly polarised. For a power-law distribution of electron energies  $N(E) \propto E^{-p}$  propagating in a uniform magnetic field, the resulting emission is polarised with fractional linear polarisation  $f = (p + 1)/(p + 7/3)$  aligned perpendicular to the magnetic field (Rybicki & Lightman 1979). The frequency dependence of synchrotron emission is also related to the electron energy distribution,  $T(\nu) \propto \nu^\beta$  with spectral index  $\beta = -(p + 3)/2$ . For  $\beta \approx -3$ , the synchrotron emission can have a maximum fractional polarisation as high as  $f_s = 0.75$ . However, line-of-sight and beam averaging effects will tend to reduce this, with typical values at high latitude of  $\sim 10$ –40%.

#### 3.2 Dust

The Galactic foreground at far-infrared and submillimetre wavelengths ( $\nu \gtrsim 100$  GHz) is dominated by thermal emission from warm ( $T \sim 10$ –100 K) interstellar dust grains. The intensity spectrum peaks in the range 100–200  $\mu$ m and is well modelled by an emissivity-modified gray-body of the form  $\nu^\beta B_\nu(T)$ , where  $B_\nu(T)$  is the Planck function at frequency  $\nu$  and temperature  $T$ . Using data at 100 and 240  $\mu$ m, Finkbeiner, Davis & Schlegel (1999) modelled the all-sky emission with two components having mean temperatures of 9.4 K and 16 K and spectral indices of  $\beta = 1.7$  and 2.7, respectively. The predictions at longer wavelengths are in good agreement with observations at 353 GHz by *Archeops* (Ponthieu et al. 2005) and at 94 GHz by *WMAP* (Bennett et al. 2003). We use the predictions at 94 GHz, which are available on the LAMBDA website, as our template for dust emission.

Polarisation from thermally emitting dust is due to aspherical grains whose spin-axes have become aligned locally with interstellar magnetic fields (e.g., see reviews by Lazarian 2003, 2007). The most efficient direction for emission and absorption/extinction is the long grain axis (perpendicular to the spin axis). The observed polarisation direction is then perpendicular to the aligning magnetic field in the case of grain emission, but parallel to the field in the case of background-starlight extinction. The expected size of the polarisation depends on a number of unknown factors including the efficiency of the alignment mechanism and the inclination of the magnetic field to the line-of-sight. Typical background-starlight polarisation has values in the  $\sim 1$ –4 % range (e.g., Heiles 2000; Fosalba et al. 2002), while polarised emission in dense Galactic clouds have been observed at 0.5–10 % (e.g., Dotson et al. 2000, 2010; Matthews et al. 2009). *WMAP* polarisation observations at 94 GHz (Page et al. 2007; Kogut et al. 2007) and *Archeops* at 353 GHz (Ponthieu et al. 2005) measure dust polarisations of  $\sim 1\%$  in the Galactic plane, increasing to a few percent at higher latitudes. Studies of the frequency dependence of polarised emission have found that the spectrum has a polarisation minimum at  $\lambda \sim 350$   $\mu$ m, increasing to longer wavelengths (e.g., Hildebrand et al. 1999). However, these studies are limited to  $\lambda = 60$ –1300  $\mu$ m and to bright/dense Galactic clouds. Extrapolating this spectrum to the conditions expected to prevail in the high-latitude diffuse ISM, one expects a more featureless spectrum for wavelengths a few times longer than about 1 mm (Hildebrand & Kirby 2004).

Other possible sources of polarised dust emission at microwave frequencies are electric-dipole emission from “spinning dust” grains, as well as magnetic-dipole emission from vibrating “magnetic dust” grains (e.g., Lazarian & Finkbeiner 2003; Draine & Lazarian 1998a,b,1999; Lazarian & Draine 2000; Al-Haimoud, Y., Hirata, C. M., & Dickinson, C. 2009). Evidence for the existence of spinning-dust exists in the strong correlations observed between the spatial distribution of thermal dust emission and that of anomalous emission at frequencies of 20–60 GHz. This anomalous emission cannot be accounted for by models using only the standard components of free-free, synchrotron, and/or thermal dust emission. This dust-correlated anomalous emission is observed on both large-scales (e.g., Kogut et al. 1996; Finkbeiner 2004; Finkbeiner, Langston, & Minter 2004; Davies et al. 2006; Hildebrandt et al. 2007; Miville-Deschênes et al. 2008) as well as in pointed observations of specific Galactic dust clouds (e.g., Finkbeiner 2004; Watson et al. 2005; Casassus et al. 2006; Dickinson et al. 2009a, 2010; Scaife et al. 2009; Planck collaboration 2011).

The polarisation amplitude of spinning-dust emission is likely to be small. Lazarian & Draine (2000), modelling the alignment of very small dust grains in the ISM, predict that spinning dust will be polarised by no more than  $\sim 7\%$  at 2 GHz, falling to  $\lesssim 0.5\%$  above frequencies of 30 GHz. Empirically, UV observations of background-starlight polarisation (caused by the same very small grains) indicate that these grains are not as well aligned with the local magnetic field as are larger grains (e.g., Martin 2007). Magnetic-dust is expected to be polarised at much higher levels, as high as 40% (Draine & Lazarian 1999). The only polarisation observations of the anomalous emission to date have found low levels. Battistelli et al. (2006) report  $3.4^{+1.5}_{-1.9}\%$  towards the Perseus molecular cloud at 11 GHz while Mason et al. (2009) report an upper limit of 3.5% (99.7% confidence level) towards the dark cloud Lynds 1622 at 9 GHz. López-Caraballo et al. (2011) used *WMAP* data to constrain the polarization towards the Perseus molecular cloud to be less than 1.0, 1.8 and 2.7 % at 23, 33 and 41 GHz, respectively.

These observations are consistent with polarisation from spinning-dust, but cannot rule out the existence of vibrating magnetic-dust.

### 3.3 Free-free

Free-free (bremsstrahlung) emission is due to electron-electron scattering from warm ( $T_e \approx 10^4$  K) ionised gas in the interstellar medium. In the optically thin regime, and at radio frequencies, the brightness temperature is given by

$$T_b = 8.235 \times 10^{-2} a T_e^{-0.35} \nu_{\text{GHz}}^{-2.1} (1 + 0.08) (\text{EM})_{\text{cm}^{-6}\text{pc}}$$

where  $T_e$  is the electron temperature, EM is the emission measure, and  $a$  is a factor close to unity. The electron temperature in the warm ionised medium ranges from  $\approx 3000$  to  $\sim 20,000$  K but is  $\approx 8000$  K at the Solar galacocentric distance. The spectrum follows a well defined power-law with a spectral index of  $-2.1$  with only a small variation in temperature. At *WMAP* frequencies, the effective free-free spectral index is  $\approx -2.14$  for  $T_e \approx 8000$  K.

The well-determined spectrum can be used to separate free-free from other diffuse radio components, most notably, synchrotron (which is almost always steeper). However, due to the complexity of the components, and limited frequency range of *WMAP*, a cleaner separation can be achieved by using an appropriate spatial template. The free-free brightness temperature is proportional to  $\text{EM} \equiv \int n_e^2 dl$ , i.e., the integrated column density squared along the line of sight. Fortunately, this is also true of recombination lines such as the bright optical line,  $\text{H}\alpha$ . Maps of  $\text{H}\alpha$  therefore give an almost one-to-one tracer for radio free-free emission (Dickinson et al. 2003) and they are now available for the full-sky (Finkbeiner 2003). There is some dependency on  $T_e$  and the local conditions, but these are relatively small. The main difficulty arises at low Galactic latitudes (typically  $|b| < 5^\circ$ ) where dust absorption can reduce the  $\text{H}\alpha$  intensity by a large factor, thus rendering it useless for predicting radio free-free brightness. However, outside the Kp2 mask, almost all lines of sight have a small to negligible maximum correction factor; typical values are  $\ll 1$  mag. The correction factor can be estimated from the IRAS  $100 \mu\text{m}$  redening maps (Schlegel et al. 1998). We therefore use the Finkbeiner (2003) composite  $\text{H}\alpha$  map as our standard free-free template, but also compare a similar map produced by Dickinson et al. (2003).

Free-free emission is intrinsically unpolarised because the scattering directions are random. However, a secondary polarisation signature can occur at the edges of bright free-free features (i.e.,  $\text{H II}$  regions) from Thomson scattering (Rybicki & Lightman 1979). This could cause significant polarisation ( $\sim 10\%$ ) in the Galactic plane, particularly when observing at high angular resolution. However, at high Galactic latitudes, and with a relatively low resolution, we expect the residual polarisation to be  $< 1\%$ .

## 4 THE CROSS-CORRELATION ANALYSIS

### 4.1 The Method

The C-C method (described in Davies et al. 2006) assumes that the total intensity in every pixel is well modelled by a finite sum of separate emission mechanisms such that

$$\mathbf{I}_{\text{tot}}(\nu, \hat{n}) = \sum_{i=1}^n T_i(\nu, \hat{n}) \quad (2)$$

$$= \sum_{i=1}^n \theta_i(\nu, \hat{n}) T_i(\nu_{0i}, \hat{n}), \quad (3)$$

where  $\mathbf{I}_{\text{tot}}(\nu, \hat{n})$  is the total emission at frequency  $\nu$  in the direction (or map pixel)  $\hat{n}$ ,  $T_i(\nu_{0i}, \hat{n})$  is the emission from the  $i^{\text{th}}$  template at the template frequency  $\nu_{0i}$  (hereafter simply  $T_i(\hat{n})$ ), and  $\theta_i(\nu, \hat{n})$  is the spectral shape of the emission template, normalised in every pixel such that  $\theta_i(\nu_{0i}) = 1$ . The C-C technique is applied to sky-regions containing different pixels and assumes that the proportionality coefficients between the total intensity and each foreground component are constant within each region. That is, the  $\theta_i(\nu, \hat{n})$  are independent of position within each region, although they can vary from region-to-region:

$$\mathbf{I}_{\text{tot}}(\nu, \hat{n}) = \sum_{i=1}^n \theta_i(\nu) T_i(\hat{n}). \quad (4)$$

For the emission mechanisms studied in this work we have  $n = 3$  templates, although the C-C method can generally be extended to any number  $n$ . For any given *WMAP* frequency  $\nu$ , an estimate of the parameters  $\theta_i(\nu)$  can be computed by minimising  $\chi^2$ , as explained in Davies et al. (2006). In the component formalism of Equation (4) we have

$$\theta_i(\nu) = \sum_{j=1}^3 (A^{-1})_{ij} \cdot \left[ \sum_{\hat{n}} (T_j(\hat{n})^T \cdot \mathbf{M}_{\text{SN}}^{-1}(\nu, \hat{n}) \cdot \mathbf{I}(\nu, \hat{n})) \right] \quad (5)$$

where the sum over  $\hat{n}$  is the sum over all pixels in sky-region  $R$ ,  $A_{ij}$  is the  $3 \times 3$  template matrix  $\sum_{\hat{n}} [T_i(\hat{n})^T \cdot \mathbf{M}_{\text{SN}}^{-1}(\nu, \hat{n}) \cdot T_j(\hat{n})]$ , and  $\mathbf{M}_{\text{SN}}(\nu, \hat{n})$  is the covariance matrix of the expected noise of the *WMAP* data and CMB signal (described in the next section). The objective is to invert the covariance matrix and compute the coefficients  $\theta_i(\nu)$  for each of the 3 Galactic foreground components.

Within an area  $R$  of the sky, the C-C analysis relies on the morphological characteristics of a given component. The mean value of the templates' emission within  $R$  (which can be thought of as a constant offset in the template's map) does not provide information for the purpose of recovering the signal relative to each individual component, as it has no morphological structure. Moreover, keeping these mean offsets in the templates fixed will bias the results of the C-C. Since all templates, as well as all five *WMAP* maps, may have such uniform offsets they can each be represented as a single uniform term in the sum of Equation (3). That is, each template and dataset have the form

$$T_i(\hat{n}) = T'_i(\hat{n}) - \delta'_i, \quad (6)$$

where  $T'$  is an existing template map or *WMAP* data, and  $T_i$  is its true value in which all constant-offsets have been removed. Equation (4) is then re-written as

$$\mathbf{I}'_{\text{tot}}(\nu, \hat{n}) = \sum_{i=1}^n \theta_i(\nu) T'_i(\hat{n}) + \delta_{\text{tot}}(\nu) \quad (7)$$

where

$$\delta_{\text{tot}}(\nu) = \delta'_{\text{tot}}(\nu) - \sum_{i=1}^n \theta_i(\nu) \delta'_i. \quad (8)$$

If each analysis is limited to a single sky region covered by a single set of parameters  $\theta_i(\nu)$  then each of the individual terms on the right-handside of Equation (8) are monopole terms. By extension, the total  $\delta_{\text{tot}}(\nu)$  must also be a constant monopole. Therefore, we can define a new template  $T_{\text{off}}(\nu, \hat{n}) \equiv T_{\text{off}} \equiv 1$  at all frequencies and all sky positions. Equation (7) can then be re-written

$$\mathbf{I}'_{\text{tot}}(\nu, \hat{n}) = \sum_{i=1}^{n+1} \theta_i(\nu) T'_i(\hat{n}) \quad (9)$$

where  $\theta_{(n+1)}(\nu) = \delta_{\text{tot}}(\nu)$  and  $T'_{(n+1)}(\hat{n}) = T_{\text{off}}$ . The C-C analysis then proceeds just as in the case of a zero-offset but simply with an additional template term, and the value of  $\delta_{\text{tot}}(\nu)$  is returned along with the other  $n$  fit parameters,  $\theta_i(\nu)$ .

The introduction of an extra fitting parameter (the amplitude of the monopole-term) increases the uncertainties returned in the other parameters of the C-C analysis. This effect is the largest at high Galactic latitudes where there is little variation in the foreground emission. That is, one should expect the correlation of the data with the monopole-template to increase with increasing latitude even if a true constant-offset does not exist in the data maps.

When these offsets are included in the C-C the reduced- $\chi^2$  is significantly better than without the offset. At K-band it decreases by about 24% for the temperature analysis and by about 8% in the analysis of the polarised emission. These offsets are found to exhibit a distinct synchrotron-like frequency spectrum, whereas one would naively expect little correlation with frequency. This suggests that the Haslam et al. 408 MHz synchrotron template is dominating the fit offset terms.

## 4.2 Uncertainties

Writing the C-C error equation following the component formalism, the uncertainties on the fitted C-C coefficients for the  $i^{\text{th}}$  template are

$$\delta\theta_i(\nu) = \sqrt{\sum_{\hat{n}}^R [(T^T(\hat{n}) \cdot \mathbf{M}_{\text{SN}}^{-1}(\nu, \hat{n}) \cdot T(\hat{n}))^{-1}]_{ii}}. \quad (10)$$

In Equation (10), the covariance matrix  $\mathbf{M}_{\text{SN}} = \mathbf{M}_{\text{S}} + \mathbf{M}_{\text{N}}$ , where  $\mathbf{M}_{\text{N}}$  and  $\mathbf{M}_{\text{S}}$  are the covariances of the instrumental noise and the CMB, respectively. The CMB signal covariance only has a significant contribution to the temperature analysis, where it dominates the instrumental noise.

We compute the signal covariance matrix in the usual way, taking the CMB power spectrum  $C_l$  from the WMAP best-fit cold-dark-matter ( $\Lambda\text{CDM}$ ) power-law spectrum model (Nolta et al. 2009). In practice, we take into account spatial correlations within  $30^\circ$  of a given pixel, effectively neglecting correlation values that are at most 0.5% that of the pixel auto-correlation. The noise covariance in intensity is determined from the uncorrelated pixel noise as specified for each pixel in the WMAP data; this is an  $N \times N$  diagonal matrix with the inverse of the observation number in each pixel on the diagonal ( $\sigma_I = \sigma_0/\sqrt{N_{\text{obs}}}$ ).

We use the same strategy as in Eq. (10) to compute the errors in the polarisation coefficients defined in Section 4.3 (Eq. 23). In the polarisation analysis the covariance matrix is dominated by the noise, which exceeds the contribution from the polarisation power spectrum  $C_l^{EE}$  by two orders of magnitude.<sup>4</sup>  $\mathbf{M}_{\text{N}}$  is, to a good approximation, a diagonal matrix as the pixel-to-pixel noise correlation is at most 1% of the diagonal term. We verified this by inspecting the  $4 \times N \times N$  complete noise matrix available at the LAMBDA website, even though this is given at  $N_{\text{side}} = 16$  and our work is done using  $N_{\text{side}} = 32$  for the reasons introduced in Section 2. While it is true that we have no information on exact pixel-to-pixel correlations at  $N_{\text{side}} = 32$ , the  $N_{\text{side}} = 16$  noise matrix suggests there are no large-scale noise correlations for the polarisation analysis.

The polarisation C-C results are, therefore, computationally

easier to determine than the temperature results, because we only need to compute  $N$ -dimensional arrays as opposed to the  $N \times N$  needed in the temperature case. Therefore, we compute the noise for the total polarisation in each pixel by combining noise in the  $Q$  and  $U$  maps at each frequency and properly taking into account  $Q$ - $U$  correlations.

In every pixel  $\hat{n}$  we have a matrix

$$N(\hat{n}) = \begin{pmatrix} QQ(\hat{n}) & QU(\hat{n}) \\ UQ(\hat{n}) & UU(\hat{n}) \end{pmatrix}$$

where  $QQ(\hat{n})$  and  $UU(\hat{n})$  are noises and  $QU(\hat{n})$  is the  $\hat{n}$  pixel  $Q$ - $U$  noise correlation, all in terms of observation number. Uncertainties on  $Q$  and  $U$  are given by the inverse of  $N(\hat{n})$

$$\begin{aligned} \sigma_q(\hat{n}) &= \sigma_0 \sqrt{[(N(\hat{n}))^{-1}]_{11}} \\ \sigma_u(\hat{n}) &= \sigma_0 \sqrt{[(N(\hat{n}))^{-1}]_{22}} \end{aligned}$$

Propagating these noise terms to compute the uncertainty on  $P = \sqrt{Q^2 + U^2}$  we obtain:

$$\sigma_p(\hat{n}) = \sqrt{\left(\frac{Q}{P}\sigma_q(\hat{n})\right)^2 + \left(\frac{U}{P}\sigma_u(\hat{n})\right)^2}. \quad (11)$$

The  $\sigma_p(\hat{n})^2$  are the elements of the (diagonal) noise matrix  $\mathbf{M}_{\text{N}}$  for the total polarisation  $P$ . The uncertainty on the polarised correlation coefficients is:

$$\delta\rho_i(\nu) = \sqrt{\sum_{\hat{n}}^R [(T^T(\hat{n}) \cdot \mathbf{M}_{\text{N}}^{-1}(\nu, \hat{n}) \cdot T(\hat{n}))^{-1}]_{ii}}. \quad (12)$$

When choosing the area over which to perform the C-C analysis, one should consider the trade-off between the uncertainties and the accuracy of the modelling. While it is more likely that in a small area a single fitting coefficient is sufficient to represent a given foreground, the uncertainties calculated with Eq. (10) and (12) decrease with the square root of the number of pixels considered. In the following, our choice to consider relatively large areas is a trade-off between these two competing aspects.

## 4.3 Polarisation analysis and fractional polarisation

When dealing with the cross-correlation of the polarised emission some preliminary comments are necessary. Since Equation (4) holds for any measured intensity and polarisation value, if templates from all Stokes parameters were available at some set of reference frequencies, i.e.,  $Q_i(\nu_{0i}, \hat{n})$  and  $U_i(\nu_{0i}, \hat{n})$ , then Equation (4) could be solved separately to determine the coefficients  $\theta_i(\nu)$  in polarisation.

That is, Equation (4), written for  $Q$  and  $U$  in each pixel  $\hat{n}$  becomes

$$Q_{\text{tot}}(\nu, \hat{n}) = \sum_{i=1}^n Q_i(\nu, \hat{n}) \quad (13)$$

$$U_{\text{tot}}(\nu, \hat{n}) = \sum_{i=1}^n U_i(\nu, \hat{n}). \quad (14)$$

Inserting the definitions of the Stokes parameters in terms of the fractional linear polarisation  $f$  and the polarisation angle  $\gamma$ ,  $Q =$

<sup>4</sup> On the diagonal elements,  $\mathbf{M}_{\text{S}} = 0.45 \mu\text{K}^2$ , while  $\mathbf{M}_{\text{N}} = 55 \mu\text{K}^2$ .

$fI \cos(2\gamma)$  and  $U = fI \sin(2\gamma)$ , Equations (13) and (14) become

$$Q_{\text{tot}}(\nu, \hat{n}) = \sum_{i=1}^n q_i(\nu, \hat{n}) T_i(\nu, \hat{n}) \quad (15)$$

$$U_{\text{tot}}(\nu, \hat{n}) = \sum_{i=1}^n u_i(\nu, \hat{n}) T_i(\nu, \hat{n}) \quad (16)$$

where the correlation coefficients are

$$q_i(\nu, \hat{n}) = f_i(\nu, \hat{n}) \theta_i(\nu) \cos[2\gamma_i(\nu, \hat{n})] \quad \text{and} \quad (17)$$

$$u_i(\nu, \hat{n}) = f_i(\nu, \hat{n}) \theta_i(\nu) \sin[2\gamma_i(\nu, \hat{n})]. \quad (18)$$

To apply C-C as we did in the temperature analysis, we assume again that the coefficients  $q_i(\nu, \hat{n})$  and  $u_i(\nu, \hat{n})$  are constant over the analysed region of the sky.

We could still apply this procedure if we had complete information about the polarisation angle for every foreground. For example, one could use simulated Galactic magnetic-field maps to estimate the position angle of a thermal-dust polarisation-template and the K-band polarisation data as a synchrotron angle template as has been done by other authors (e.g., Dunkley et al. 2009; Page et al. 2007).

In this work we wish to determine if useful knowledge can be extracted from the *WMAP* polarisation data without making any assumptions about the dust or synchrotron polarisation angles. It is possible to do so by considering the total polarisation

$$P_{\text{tot}}^2(\nu, \hat{n}) \equiv f^2(\nu, \hat{n}) T^2(\nu, \hat{n}) = Q^2(\nu, \hat{n}) + U^2(\nu, \hat{n}) \quad (19)$$

$$= \left( \sum_{i=1}^n q_i(\nu, \hat{n}) T_i(\hat{n}) \right)^2 + \left( \sum_{i=1}^n u_i(\nu, \hat{n}) T_i(\hat{n}) \right)^2. \quad (20)$$

Equation 20 can be re-written by replacing  $q_i$  and  $u_i$  using Equations (17) and (18) so that

$$P_{\text{tot}}^2(\nu, \hat{n}) = \sum_{i=1}^n f_i^2 \theta_i^2 T_i(\hat{n})^2 + \sum_{i=1}^n \sum_{j=1, j \neq i}^n f_i f_j \theta_i \theta_j T_i(\hat{n}) T_j(\hat{n}) \cos[2(\gamma_i(\hat{n}) - \gamma_j(\hat{n}))]. \quad (21)$$

(Note that we have dropped the frequency-dependence in Equation [21] for simplicity only.) If we further assume that the polarisation angles are equal for all emission components ( $\gamma_i(\hat{n}) = \gamma_j(\hat{n})$ ) then

$$P_{\text{tot}}(\nu, \hat{n}) = \sum_{i=1}^n \rho_i(\nu) T_i(\hat{n}) \quad (22)$$

where

$$\rho_i(\nu) \equiv f_i(\nu) \theta_i(\nu). \quad (23)$$

Equation (22) is analogous to Equation (4), but with the polarised-intensity correlation coefficients  $\rho_i(\nu)$  rather than  $\theta_i(\nu)$ . Therefore,  $\rho_i(\nu)$  can be computed by analogy with the C-C used to calculate the  $\theta_i(\nu)$  given by Equation (5). The fractional polarisation coefficient  $f_i(\nu)$  can be extracted for each component at each frequency from these two correlation coefficients:

$$f_i(\nu) = \frac{\rho_i(\nu)}{\theta_i(\nu)}, \quad (24)$$

with an uncertainty of:

$$\delta f_i(\nu) = f_i(\nu) \times \sqrt{\left( \frac{\delta \rho_i}{\rho_i} \right)^2 + \left( \frac{\delta \theta_i}{\theta_i} \right)^2} \quad (25)$$

The assumption of an equal polarisation angles for all emission components is reasonable because the direction of all diffuse emission types is determined by the direction of the magnetic field. This assumption leads to a total polarisation (summed over all emission components) with angles equal to the individual components, so that it is easily falsifiable by any measurement in which the total position angle changes with frequency. While such angle rotations with frequency are observed in the *WMAP* data they are typically smaller than  $\sim 20^\circ$  at a resolution of  $4^\circ$ . Moreover, the nearly-constant angle assumption is supported by Kogut et al. (2007) who found that the fits based on K-band (synchrotron-dominated) polarisation angles or the starlight-polarisation angles gave similar results, with a difference in the goodness-of-fit of about 1%. The advantage of our approach is that no models are required to estimate the polarisation angles.

The fractional polarisation  $f_i(\nu)$ , as given in Equation (24), is the ratio of *correlation coefficients*. One should keep in mind that negative values of the correlation coefficients  $\rho_i(\nu)$ , and therefore  $f_i(\nu)$ , are in fact physically meaningful. Anti-correlations between the polarisation data and a total intensity template will occur in regions where the polarised emission drops with increasing total intensity. For example, this behaviour can be expected in regions where the polarisation drops due to increased line-of-sight averaging towards regions of increasing column density. This point provides another reason to consider small areas of the sky where the polarisation fraction is more likely to be constant.

#### 4.4 Polarisation noise bias

Given the  $Q$  and  $U$  values in each pixel, we calculate the polarised intensity using

$$P(\hat{n}) = \left( \langle Q \rangle^2(\hat{n}) + \langle U \rangle^2(\hat{n}) \right)^{1/2}, \quad (26)$$

and its associated uncertainty, where the direction  $\hat{n}$  denotes each  $N_{\text{side}} = 32$  ( $\approx 2^\circ \times 2^\circ$ ) piece of sky. The correlation analysis is then carried out on the  $P(\hat{n})$  in each section of the sky defined in Section 5.

The polarisation is a complex quantity which can be described by either its real and imaginary parts ( $Q$  and  $U$ ), or its amplitude and phase ( $P$  and  $\gamma$ ). If one assumes gaussian statistics for  $Q$  and  $U$ , then the non-linear transformation into  $P$  and  $\gamma$  results in non-gaussian statistics for these quantities. The key point for our analysis is that  $P$  has an asymmetric probability distribution (e.g., Vaillancourt 2006; Simmons & Stewart 1985) resulting in a positive bias. We have corrected for this bias using the formula:

$$P_{\text{true}} = 0 \quad \text{for } P/\sigma_P < \sqrt{2} \quad (27)$$

$$P_{\text{true}} \approx \sqrt{P^2 - \sigma_P^2} \quad \text{for } P/\sigma_P > \sqrt{2} \quad (28)$$

where  $\sigma_P$  is the polarisation uncertainty defined in Section 4.2. While the last expression is not exactly precise one can limit the effects of the bias by only using data above some polarisation signal-to-noise level.<sup>5</sup> Such a bias can be estimated using monte carlo simulations as described in Section 5.1.

<sup>5</sup> No bias-correcting algorithm is exact. For more information see Simmons & Stewart (1985), Vaillancourt (2006), and references therein.

## 5 RESULTS

We used C-C to compute, at each *WMAP* band, the emission coefficients of the three Galactic foreground components plus the offset monopole template. The analysis presented in this work was done in three different spatial configurations: on the whole sky outside of the KQ85 Galactic mask (hereafter the “all-sky” analysis), in different isolatitude slices (hereafter the “latitude” analysis) with  $b = -90^\circ / -50^\circ$ ,  $-50^\circ / -20^\circ$ ,  $-20^\circ / 20^\circ$ ,  $20^\circ / 50^\circ$ ,  $50^\circ / 90^\circ$ , and in 48 HEALPix  $N_{\text{side}} = 2$  regions (hereafter the “pixel” analysis). Selecting such partitions allows us to investigate how the foreground properties depend on direction and latitude (see also Kogut et al. 2007; Miville-Deschênes et al. 2008), while increasing the likelihood that the area we are analysing has a uniform fractional polarisation (see Section 4.3). The best pixel area size among those tried is  $N_{\text{side}} = 2$ ; it is small enough that the assumption of constant polarisation fraction is more likely to be satisfied, and large enough to contain spatial variations needed for the C-C method. Moreover, these areas match with previous works (e.g. Dunkley et al. 2009) allowing us to compare our results. Fig. 1 shows the sky-locations of pixels used for the pixel-analysis and the latitude slices used for the latitude-analysis (see Table 3 for the mean latitudes and longitudes of each pixel).

From the C-C coefficients we derive results on the relative level of each foreground in a given region, its frequency dependence in temperature and polarisation, and its polarisation fraction. We note here that it is not always possible to extract all this information at all frequencies and for all regions due to limited signal-to-noise ratios. Therefore, we concentrate on results where there is  $2\sigma$  statistical significance.

### 5.1 Tests on a simulated sky

In order to test the analysis method described in the preceding sections, we ran the CCA code on 500 noise realisations of a simulated sky with a given foreground parametrisation. We created sky maps in both temperature and polarisation, based on the three template temperature maps from Section 3 and scaled them using the average coefficients from Davies et al. (2006) at each frequency. We used a constant polarisation fraction of 20% for synchrotron, 3.5% for dust<sup>6</sup>, and 0% for free-free and a polarisation angle for both synchrotron and dust based on the *WMAP5* K-band map. We also made a set of simulations with no dust polarisation to compare cases without and without dust polarisation. The CMB model is a Gaussian realisation based on the *WMAP5* concordance model. We used the LAMBDA  $N_{\text{side}} = 512$   $I$ ,  $Q$ , and  $U$  inverse covariance matrices to produce a  $N_{\text{side}} = 512$  noise realisation, which was added to the CMB and foreground maps, and then degraded to the resolution used in our analysis, i.e.,  $N_{\text{side}} = 32$ .

We compared the results for each of the three components for the 500 realisations in each pixel. We focused on the results from K-band, where the data had the most significance. The recovered coefficients were, in general, close to the input values with no large biases. In temperature, the results were all within  $3\sigma$  of the input value, except for one region for synchrotron (region 10 at  $3.3\sigma$ ) and one region for dust (region 12 at  $3.1\sigma$ ). The estimated uncertainties corresponded well to the scatter in the coefficients from the 500 realisations.

<sup>6</sup> The 3.5% polarisation represents the polarisation for the total dust-correlated component at K-band, which will be dominated by anomalous microwave emission, and virtually no contribution from thermal dust.

In polarisation, the results for synchrotron and free-free were in good agreement with the input values. The mean recovered fractional polarisation for synchrotron was  $20.0 \pm 0.3\%$  for the case with no dust polarisation and  $19.5 \pm 0.3\%$  with dust polarisation. For free-free, we obtained mean values of  $-0.02 \pm 0.18\%$  and  $-0.04 \pm 0.19\%$  for each case, respectively. This gives us confidence that the method works as expected and yields reasonable results.

However, the values recovered for dust did indicate bias i.e. an additional systematic error. The recovered fractional polarisation was  $0.003 \pm 0.15\%$  and  $0.38 \pm 0.15\%$  for the simulations with no dust polarisation, and 3.5% dust polarisation, respectively. This shows that simply averaging all the polarisation values within a pixel will not yield a reliable estimate if the true value is as low as a few percent. The situation improves when only using regions with significant ( $> 2\sigma$ ) detections. We found 9 regions that were significant at the  $2\sigma$  level, which resulted in a weighted average of  $2.0 \pm 0.2\%$ , i.e., an underestimate by 1.5% in absolute value. For the case with no dust polarisation, no pixels were detected at greater than the  $2\sigma$  level. Similarly, for free-free, we obtained an average value of  $1.4 \pm 0.4\%$  when using the 6 regions that were significant, i.e., an overestimate of 1.4% in absolute value.

From these tests, we conclude there is a bias in the average fraction polarisation of  $\approx 1.5\%$ , when the true fractional polarisation is a few percent or less. For a single region, we found cases where the bias is up to  $\approx 5\%$ . The reason for this bias appears to lie in cross-talk between the various components. For example, for regions we recover a significant dust polarisation, with no dust polarisation in the simulation, one can see a bias in either the synchrotron or free-free polarisation; this can explain why the average synchrotron polarisation is slightly low, at the  $1.7\sigma$  level, in the case where there is dust polarisation. Nevertheless, we can still obtain useful constraints on the fractional polarisation with the current data, keeping in mind the amplitude of possible biases.

Also, we can use the results of these simulations to estimate the significance of results for individual pixels. These will be discussed separately, in the following sections on the synchrotron, free-free and dust results. For the cases where there is significant bias observed in the simulations, the fractional polarisation results will be presented in terms of a statistical (stat) and systematic (sys) error. For example, for the significant dust regions above, the weighted average is  $2.0 \pm 0.2$  (stat)  $\pm 1.5$  (sys) %.

### 5.2 All-sky versus pixel analysis

We show in Fig. 2 the contribution of each foreground to the temperature emission as a function of frequency. These estimates, reported in Table 1, were obtained by multiplying the C-C coefficient for a given foreground at a given frequency with the root-mean-square (r.m.s) of each foreground template outside the KQ85 mask. The figure clearly shows that the dust-correlated emission is the dominant component in temperature at all frequencies (see also Davies et al. 2006). The rise from 61-to-94 GHz indicates the high frequency contribution of thermal dust, while at lower *WMAP* frequencies, there is a significant contribution from anomalous dust. It is this low frequency dust-correlated emission that has been tentatively identified with emission from small rapidly-spinning dust grains (Draine & Lazarian 1998a,b). However, the dust contribution to polarisation is typically subdominant at low frequencies and will be discussed further in Section 5.4.

Given the C-C coefficients and foreground templates, and the assumption that the templates trace all the foreground emission, we



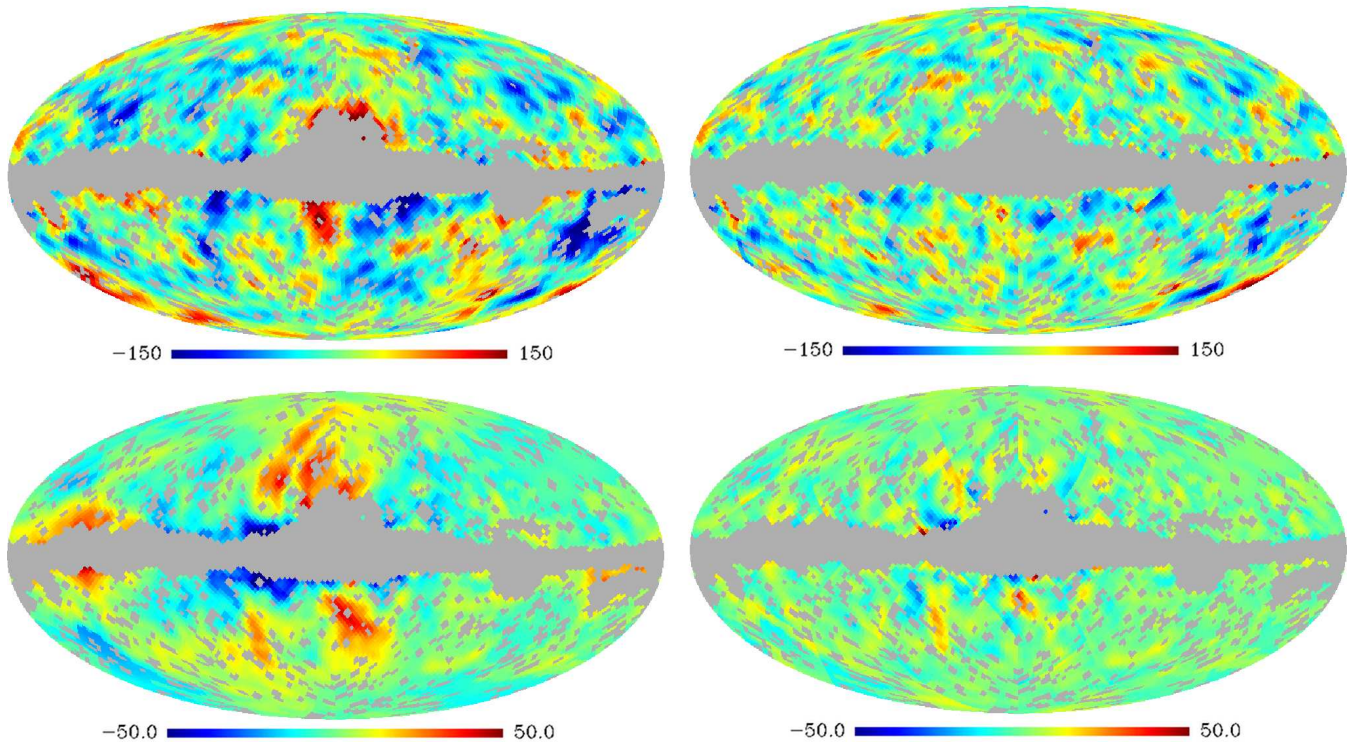


**Figure 3.** Residual maps (on mollweide projection) for the *WMAP* K-band temperature (*top*) and polarised intensity (*bottom*) analyses. The results using the all-sky (KQ85 cut) region are reported (*left*) together with the results using the 48 HEALPix  $N_{\text{side}} = 2$  regions (*right*). The units of the color-scale are  $\mu\text{K}$ .

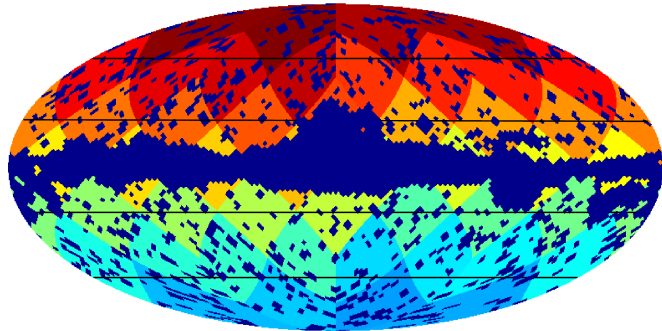


**Figure 1.** All-sky map with the 48 HEALPix  $N_{\text{side}} = 2$  regions in different colours with the KQ85 mask applied (dark blue). Horizontal black lines represent the isolatitude slices (latitude analysis) with  $b = -90^\circ / -50^\circ, -50^\circ / -20^\circ, -20^\circ / 20^\circ, 20^\circ / 50^\circ, 50^\circ / 90^\circ$ .

can generate a model of the total foreground emission in the *WMAP* data. Comparing this model to the actual *WMAP* data yields a set of residuals which we use to estimate the extent to which a single fit-coefficient (in the case of the all-sky analysis) represents the foregrounds across the whole sky. Results for the K-band, where the foregrounds are the brightest, are reported in Fig. 3(*left*) for both temperature and polarisation. In the all-sky temperature residuals, the largest residuals occur near the Galactic plane, particularly near the Galactic centre. This feature has been interpreted as the Galactic haze, possibly associated with annihilating particles (Finkbeiner et al. 2004; Cumberbatch et al. 2009). However, this feature is not

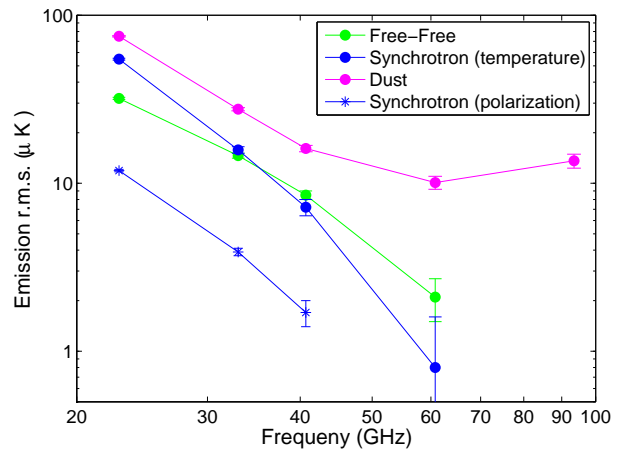


**Figure 2.** R.M.S. emission spectrum of Galactic foreground components from the all-sky (KQ85 cut) intensity and polarisation analysis, in  $\mu\text{K}$ . Only the polarised synchrotron emission is plotted as the dust-correlated and free-free-correlated polarised emission are consistent with zero for the all-sky region.

evident in the pixel-analysis where we compute separate C-C coefficients in 48 different regions (Fig. 3(*right*)). This is a consequence of a varying synchrotron spectral index, which is somewhat flatter than average near the Galactic centre, due to a diversified population of electrons in the Galaxy.

Bright residuals in the all-sky analysis are also concentrated on the well-known Galactic spurs such as the North-Polar Spur (NPS) above and below the Galactic centre region. These spurs are



	K-band	Ka-band	Q-band	V-band	W-band
<b>Temperature r.m.s. emission [<math>\mu K</math>]</b>					
S	54.8 $\pm 0.7$	15.8 $\pm 0.7$	7.2 $\pm 0.8$	0.8 $\pm 1$	-0.8 $\pm 1.3$
D	75.0 $\pm 0.6$	27.6 $\pm 0.6$	16.1 $\pm 0.7$	10.1 $\pm 0.9$	13.6 $\pm 1.3$
F-F	32.0 $\pm 0.5$	14.6 $\pm 0.5$	8.5 $\pm 0.5$	2.0 $\pm 0.6$	-0.2 $\pm 1.1$
<b>Polarisation r.m.s. emission [<math>\mu K</math>]</b>					
S	11.9 $\pm 0.2$	3.9 $\pm 0.2$	1.7 $\pm 0.3$	0.1 $\pm 0.4$	0.1 $\pm 0.4$
D	-0.2 $\pm 0.1$	-0.1 $\pm 0.2$	0.0 $\pm 0.3$	0.1 $\pm 0.3$	0.0 $\pm 0.4$
F-F	-0.2 $\pm 0.1$	-0.3 $\pm 0.2$	-0.2 $\pm 0.2$	0.0 $\pm 0.4$	0.0 $\pm 0.6$

**Table 1.** Emission r.m.s. values for the all-sky analysis in both temperature and polarisation for synchrotron (S), dust (D), and free-free (F-F) in the five WMAP bands. These values are plotted in Fig. 2.

	K-band	Ka-band
All-Sky Temperature	0.94	0.68
All-Sky Polarisation	5.37	0.73
Latitude Temperature	0.97	0.74
Latitude Polarisation	3.72	0.56
Pixels Temperature	0.65	0.48
Pixels Polarisation	1.65	0.30

**Table 2.** Reduced- $\chi^2$  for the three analysis types implemented in the paper. The values are the average over the different regions (when more than one is used).

known to have a slightly steeper synchrotron spectral index than average and, therefore, are not well suited for the all-sky polarisation analysis. Furthermore, these large coherent features are expected to have significantly different fractional polarisations. The residual map for the 48 pixel-analysis (Fig. 3) shows less extended structure, with more localised residuals near the mask edge. This indicates that a local analysis is more suited to handle the complex foreground variations. In summary, Fig. 3 shows that it is suboptimal to model foregrounds without considering that they are spatially varying in the sky.

To have a quantitative understanding of the goodness-of-fit we compute the reduced- $\chi^2$  for each type of analysis, both in temperature and polarisation. These are reported for the WMAP K- and Ka-bands in Table 2. Again we see that neither the all-sky nor the latitude analyses are as accurate as the pixel-analysis, especially in the K-band polarisation. A limitation of the pixel-analysis is that, in any given pixel, there may not be sufficient data points to yield a signal-to-noise ratio larger than 1. This is a particular problem for high frequencies (mostly V- and W-bands) in polarisation. In most cases we will be limited to studying the WMAP foregrounds at K-band only. The 48 emission coefficients in K-band, for each foreground component in intensity and polarisation, are reported in Table 3.

### 5.3 Synchrotron

Synchrotron is the dominant contribution to the polarised K- and Ka-band emission, especially in the northern hemisphere, as reported in Table 3, because of the strong emission associated with the north polar spur. On the other hand, synchrotron is comparable to anomalous dust emission in temperature, and again its emission is more intense in the northern part of the sky.

From the all-sky analysis, using K- and Ka- band and the corrected Haslam et al. map described before, we find  $\beta_s = -3.32 \pm 0.12$  in intensity and  $\beta_s = -3.01 \pm 0.03$  in polarisation, where the errors come from the uncertainties on the C-C coefficients. The smaller polarisation uncertainties occur here because synchrotron

is the dominant polarised foreground at low frequencies, as opposed to the intensity analysis where the dust-correlated and free-free-correlated emission are comparable to the synchrotron. These synchrotron spectral indexes are in good agreement with previous results, i.e.  $\beta_s \approx -3$  (e.g. Miville-Deschênes et al. 2008).

From the pixel analysis we find that the synchrotron emission is polarised from  $\approx 5\%$  in some regions at low Galactic latitude up to  $\approx 40\%$  at high latitudes, as reported in Fig. 4 (top). In Fig. 5 the same quantity is plotted as a function of the mean Galactic latitude of each region. The decline of the polarised emission at low latitudes is well known in the literature (e.g., Wolleben et al. 2006) and is interpreted as a depolarisation effect near the Galactic plane ( $|b| \lesssim 20^\circ$ ) due to integration along the line-of-sight of emission with different polarisation angles. The average polarisation fraction in the pixel regions with ( $|b| < 20^\circ$ ) is  $8.6 \pm 1.7$  (stat)  $\pm 0.5$  (sys) %. Uncertainties at high latitudes are usually larger than at low latitude because the templates have less variations in their structure at high latitudes. This renders the C-C analysis increasingly degenerate, as explained in Section 4.2. Nevertheless, the synchrotron fractional polarisation at high Galactic latitude is in the range  $\sim 10 - 40\%$  with an average value of  $19.3 \pm 0.8$  (stat)  $\pm 0.5$  (sys) % and standard deviation of  $\pm 11.0\%$  ( $|b| > 20^\circ$ ). As discussed in Section 5.1, the synchrotron values are the most robust of the three components, and we believe the errors from the C-C method are representative, even after averaging.

Our estimate of the synchrotron fractional polarisation is consistent with other work at the  $1\sigma$  level. Kogut et al. (2007) computed the fractional synchrotron polarisation by dividing the polarised emission (estimated using a pixel-by-pixel frequency fit), by a synchrotron intensity map (based on a MEM analysis; Hinshaw et al. 2007). They find a typical fractional synchrotron polarisation of 5–25 %. However, since this intensity map was computed ignoring a possible contribution from anomalous dust, the synchrotron intensity may be overestimated, resulting in an underestimate of the fractional polarisation. On the other hand, Miville-Deschênes et al. (2008) included a spinning-dust contribution to the total K-band intensity, and obtained a higher synchrotron fractional polarisation, up to 40%. The fact that our results are compatible with these implies that in most of the pixel regions the assumptions described in Section 4.3 are reasonable.

We have computed the synchrotron spectral index in every pixel with a S/N ratio  $> 2$  again using only the K- and Ka-bands; see Table 4. The problem in this case is that the pixels with S/N ratio  $> 2$  are few, and we conclude that the C-C technique is not appropriate for a detailed spectral-index analysis. Nonetheless, the spectral indices in polarisation are consistent with other analyses (e.g., Dunkley et al. 2009) who find  $\beta_s \simeq -3$ ; we find an average value is  $\beta_s = -3.24 \pm 0.20$ .

In temperature, the results are not compatible with polarisation, with an average spectral index of  $\beta_s = -2.02 \pm 0.20$ . This is clearly too flat and must be an artifact of the analysis. We checked that these results, especially in the 5 low  $\beta_s$  regions, are not due to a high correlation between synchrotron and dust. Without sufficient differences in spatial morphology between synchrotron and dust, confusion can occur between the two components in the C-C. As we expected, the dust and synchrotron templates are correlated with an all-sky (outside the KQ85 mask) correlation coefficient of  $r = 0.48$ . In the regions where high synchrotron spectral indices are observed (4, 5, 16, 27 and 32) the correlation between dust and synchrotron is higher ( $r = 0.71$ ). This suggests again that, in temperature, the C-C in some pixel regions is not able to correctly separate the synchrotron, free-free and dust components. In fact,

Pixel	Pixels	$\langle \text{Lat} \rangle$	$\langle \text{Long} \rangle$	Synch K	Dust K	Dust W	Synch %	Dust %	F-F %	$\chi^2_T$	$\chi^2_P$
1	207	65.7	46.2	$38.9 \pm 3.8$	$19.6 \pm 4.2$	$11 \pm 5.3$	<b>40.6</b> $\pm 4.7$	$< 11.0$	—	0.45	0.41
2	214	66.7	134.8	—	—	—	—	—	—	0.31	0.81
3	214	66.8	224.5	—	$9.5 \pm 3.2$	—	—	—	—	0.49	0.73
4	202	67	318	$30.6 \pm 3.4$	$9.5 \pm 3.4$	—	<b>23.8</b> $\pm 3.6$	—	$< 11.6$	0.84	0.41
5	189	42.3	21.3	$49.5 \pm 3.3$	$56.8 \pm 4.3$	—	<b>26.1</b> $\pm 2.4$	<b>7.2</b> $\pm 2.3$	—	0.45	3.01
6	195	43	69.7	—	$19.9 \pm 3.2$	$6.2 \pm 3.5$	—	<b>10.6</b> $\pm 4.9$	—	0.49	2.11
7	209	42	110.3	$9.9 \pm 2.6$	$32.7 \pm 3.4$	$7.4 \pm 3.7$	<b>17.8</b> $\pm 7.5$	$< 5.0$	—	0.55	0.75
8	195	41.9	159.8	$10.2 \pm 4.5$	$30.8 \pm 4.3$	$8.4 \pm 4.8$	$42.4 \pm 21.6$	$< 7.6$	—	0.49	1.42
9	211	41.7	200.1	$8.7 \pm 3.7$	—	—	$16.7 \pm 14.4$	—	—	0.56	0.22
10	232	41.6	250.8	$12.9 \pm 3.4$	$12.8 \pm 2.8$	—	<b>18.3</b> $\pm 7.6$	$< 12.8$	$< 12.4$	0.60	0.31
11	205	42.1	289.8	$16.8 \pm 2.9$	$23.8 \pm 3.4$	—	<b>21.3</b> $\pm 6.2$	—	$< 11.6$	0.47	1.05
12	214	42.4	339.6	$25.7 \pm 4.1$	$43.5 \pm 4.2$	—	<b>22.5</b> $\pm 5.6$	$< 5.8$	—	0.37	2.16
13	44	30.9	4.1	$21.1 \pm 4.5$	<b>69.6</b> $\pm 4.9$	$14.1 \pm 5.2$	<b>44.3</b> $\pm 12.8$	$< 3.6$	$< 6.4$	1.32	2.32
14	200	21.1	44.9	<b>104.8</b> $\pm 4.4$	$54.7 \pm 4.3$	—	<b>23.7</b> $\pm 1.4$	—	—	0.98	2.02
15	158	21.4	88.6	—	<b>110.5</b> $\pm 3.4$	$17.2 \pm 3.4$	—	$< 1.6$	$< 5.0$	0.63	1.87
16	167	22.7	135	<b>81.9</b> $\pm 5.3$	<b>76.4</b> $\pm 4.2$	—	<b>19.8</b> $\pm 1.9$	—	$7.6 \pm 4.8$	0.61	0.28
17	211	20.1	180.5	$22.9 \pm 3.9$	<b>80</b> $\pm 3.4$	$20.9 \pm 4.0$	<b>29.6</b> $\pm 6.9$	$2.6 \pm 1.3$	—	2.25	1.39
18	209	20.3	225.1	—	<b>62.1</b> $\pm 4.3$	<b>26.8</b> $\pm 4.4$	—	$< 2.4$	—	1.10	0.43
19	172	22.6	270.4	$12.2 \pm 4.4$	$22.9 \pm 3.7$	—	<b>34.9</b> $\pm 16.2$	$< 9.8$	$< 3.8$	1.26	1.22
20	162	22.9	315	<b>97.3</b> $\pm 3.5$	$45.2 \pm 4.6$	—	<b>14.8</b> $\pm 1.1$	$< 7.2$	—	0.52	2.10
21	28	-8.1	23.5	<b>59.7</b> $\pm 5.9$	$54.3 \pm 7.2$	—	—	$8.4 \pm 5.9$	—	0.81	6.08
22	86	0	66.1	$48.3 \pm 6.7$	<b>61.2</b> $\pm 5.2$	—	$5.7 \pm 3.4$	$< 5.0$	$< 6.0$	0.50	5.14
23	50	-5.9	110.4	$33.1 \pm 5.4$	<b>84.1</b> $\pm 6.4$	—	<b>10.8</b> $\pm 5.1$	<b>6.0</b> $\pm 1.8$	$< 7.0$	0.78	1.33
24	53	6.3	158.1	$12.8 \pm 6.2$	<b>102.5</b> $\pm 6.1$	$29.4 \pm 7.2$	$43.9 \pm 26.9$	$2.3 \pm 2$	—	0.57	1.30
25	88	5.6	203.6	—	<b>100.9</b> $\pm 5.3$	<b>22.7</b> $\pm 6.0$	—	$2.8 \pm 1.8$	$8.7 \pm 5.1$	1.78	0.84
26	64	3	244.4	$11.7 \pm 7.6$	$54.3 \pm 5.5$	—	—	$< 5.8$	$< 3.2$	1.15	0.46
27	74	-0.8	291.3	<b>58.2</b> $\pm 4.7$	<b>60.1</b> $\pm 4.3$	—	<b>9.1</b> $\pm 2.2$	$2.7 \pm 1.7$	$< 12.6$	0.90	1.11
28	16	-12.2	336.7	<b>88</b> $\pm 17.2$	$35.8 \pm 16.2$	—	—	—	—	0.88	2.80
29	180	-22.3	1.5	<b>62.5</b> $\pm 4.9$	<b>64.9</b> $\pm 3.5$	$13.8 \pm 4.1$	<b>19.6</b> $\pm 2.6$	—	—	0.47	0.49
30	214	-21	45.2	$39.7 \pm 5.6$	<b>74.4</b> $\pm 5.6$	$15.8 \pm 5.6$	$6.8 \pm 3.6$	$< 4.0$	—	1.00	2.20
31	177	-21.8	89.4	—	<b>88.1</b> $\pm 3.6$	<b>28.3</b> $\pm 4.4$	—	$< 2.0$	—	0.49	0.81
32	195	-19.9	135.2	$34.2 \pm 4.7$	<b>80</b> $\pm 4.1$	$12.6 \pm 4.6$	<b>36.9</b> $\pm 6$	$1.5 \pm 1.4$	$< 6.2$	0.99	1.17
33	102	-24.9	178	$17.8 \pm 3.5$	<b>107.1</b> $\pm 3.8$	<b>30.2</b> $\pm 4.0$	<b>52.9</b> $\pm 12.5$	$< 2.4$	$< 6.0$	1.13	0.82
34	150	-20.5	226.9	<b>72.6</b> $\pm 6.4$	<b>104.8</b> $\pm 5.2$	<b>22.7</b> $\pm 7.4$	<b>7.1</b> $\pm 2.3$	<b>3.2</b> $\pm 1.5$	$< 10.2$	0.45	0.85
35	145	-22.2	272.1	—	$51.1 \pm 5.2$	—	—	<b>4</b> $\pm 1.8$	$< 2.2$	0.50	0.74
36	181	-21	314	$39 \pm 4.6$	<b>79.3</b> $\pm 3.5$	$14.3 \pm 4.4$	<b>26.4</b> $\pm 4.2$	$< 2.2$	—	0.49	1.23
37	207	-41.8	19.3	$24.7 \pm 4.5$	$18.7 \pm 6$	—	<b>21.6</b> $\pm 6.6$	—	—	0.39	0.61
38	191	-42.7	69.6	—	$25.3 \pm 3$	—	—	$< 6.6$	—	1.05	2.12
39	206	-41.9	109.9	$10.8 \pm 3.7$	$16.4 \pm 2.4$	—	—	$< 10$	—	0.47	0.60
40	202	-42	159.8	—	<b>90.5</b> $\pm 3.2$	—	—	$< 2.6$	—	0.98	1.09
41	213	-42.8	200	—	$47.8 \pm 2.6$	$7.2 \pm 2.8$	—	$< 3.8$	$< 8.4$	1.27	0.80
42	201	-42.2	251.1	—	$13.8 \pm 4.4$	—	—	—	—	0.59	0.96
43	217	-42.4	290.5	—	<b>66</b> $\pm 4$	<b>15.7</b> $\pm 4.4$	—	$< 2.2$	$< 10.6$	0.33	0.70
44	215	-41.6	339.7	$33.8 \pm 4.2$	$13.1 \pm 4.3$	—	<b>38.5</b> $\pm 5.6$	—	—	0.56	1.30
45	203	-66.4	45.7	$11.8 \pm 2.8$	$11.5 \pm 3.2$	—	<b>25.2</b> $\pm 9.1$	<b>31.7</b> $\pm 11.7$	—	0.40	0.32
46	202	-66.3	134.4	$20.5 \pm 2.9$	—	—	—	—	—	0.55	1.60
47	206	-66.7	224.2	$10.3 \pm 3.6$	$12.7 \pm 2.5$	—	$13.8 \pm 8.8$	$< 9.8$	—	0.91	0.72
48	193	-65.7	313.6	—	—	—	—	—	—	0.37	0.63

**Table 3.** Results of the pixel analysis. Here we report the pixel region number, the number of data points, the average latitude and the average longitude of each region, the synchrotron-correlated temperature emission at K-band in  $\mu\text{K}$ , the dust-correlated temperature emission at K-band and at W-band in  $\mu\text{K}$ , and fractional polarisation percentage of synchrotron, anomalous dust and free-free at K-band. Bold faces are used to emphasise a component with a temperature emission higher than  $60 \mu\text{K}$  at K-band and  $15 \mu\text{K}$  at W-band, and are used to indicate regions where a particular component is found to be more than  $2\sigma$  significantly polarised. We indicate  $2\sigma$  upper limits when in that region the fractional polarisation is compatible with zero. No data for fractional polarisations indicates upper limits reaching 100%. In column 5, 6 and 7 we display detections that are significant at the  $1\sigma$  level. Note that the systematic uncertainties are not included here and can be significant when the polarisation fractions are low, i.e. less than a few per cent (see Section 5.1). The  $\chi^2$  values from temperature and polarisation analysis at K-band are also reported.

most of the areas where the spectral index is biased by this effect are the ones that have problems for synchrotron in our simulations, e.g. regions 16, 27, 32. Moreover, when fitting over larger regions, the spectral index moves to more typical values of  $\beta_s \approx -3$ . The same difficulty with C-C analysis was found in previous work, e.g. Davies et al. (2006), where the introduction of the 0.4 GHz point of Haslam et al. was needed to obtain meaningful spectral index

values. However, we note that this problem is most significant at the higher frequency channels above 33 GHz while K-band the coefficients are not strongly affected. Indeed, the spectral index computed from the weighted mean K-band coefficient alone, which corresponds to the mean spectral index between 408 MHz and 23 GHz, is  $\beta = -2.97 \pm 0.01$ .

Pixel	$\beta_s$ Temperature	$\beta_s$ Polarisation
1	$-2.88 \pm 0.92$	$-3.01 \pm 0.56$
4	$-1.79 \pm 0.65$	$-3.58 \pm 0.98$
5	$-1.85 \pm 0.41$	$-3.39 \pm 0.64$
14	$-2.02 \pm 0.30$	$-3.44 \pm 0.41$
15	—	$-3.22 \pm 0.95$
16	$-1.35 \pm 0.34$	$-3.50 \pm 0.89$
20	$-2.28 \pm 0.25$	$-4.13 \pm 0.94$
21	$-2.30 \pm 0.73$	—
22	—	—
27	$-1.48 \pm 0.45$	—
28	—	—
29	—	$-2.81 \pm 0.99$
32	$-1.73 \pm 0.92$	$-2.53 \pm 0.71$
44	—	$-3.36 \pm 0.82$

**Table 4.** Synchrotron spectral index values in different pixel regions from the intensity and polarisation analyses at K- and Ka-bands. Only the regions with a significant result are reported ( $\sigma_{\beta_s} < 1.0$ ).

#### 5.4 Dust

It is clear from the all-sky analysis of Fig. 2 that the total unpolarised signal across all 5 *WMAP* bands is dominated by dust-correlated emission. The rise in dust emission from 61 to 94 GHz is consistent with the expectation of thermally emitting dust. The drop with frequency from 22 to 61 GHz has been termed “anomalous” dust-correlated emission and has been attributed to such sources as spinning-dust emission (e.g., Lazarian & Draine 1998a,b) and dust-correlated synchrotron emission (Bennett et al. 2003). The results in Fig. 2, and K–Ka spectral index for anomalous dust of  $\beta_d \approx -2.5$ , is consistent with the results of Davies et al. (2006).

The results for emission presented in Table 3 show that dust emission also dominates the unpolarised K-band emission for most of the sky in the pixel-analysis. We find that the dust-correlated emission is dominant at low frequencies in many pixels even where the thermal dust emission is not present, (e.g., pixels 16, 22, 23, 27, and 40).

Fig. 4 shows the polarisation fraction of each foreground at K-band, computed using Equation (24). The same values are reported in Table 3. As expected, synchrotron emission is highly polarised, while dust and free-free almost unpolarised. We compared the values found in various pixels with the distributions obtained from simulations. As a general comment on the simulations we can say that a) the range of the recovered dust polarisation fraction, assuming the null hypothesis, is typically 5–10 % and varies between a few percent and 25% (for regions very distant from the Galactic plane, e.g., 2, 3, 47, 48); b) the distributions from simulations with and without dust polarisation are, in general, very similar, although higher mean polarisation values are not always associated with the case corresponding to the polarised dust (this may indicate cross-talk with other components); c) the variance in the distributions is typically similar to the error bars computed by the CCA on real data.

When we compare the detected values of the polarisation fraction in the K-band with the distribution we find that in some pixels they exceed the tail of the simulation distribution. The pixels for which the simulation-recovered values are always below the (real) detected dust polarisation are 5, 17, 21, 23, 25, 27, 34, 35 (see examples in Fig. 7)<sup>7</sup>. In some regions (5, 6, 17, 21, 23, 24,

<sup>7</sup> For comparison, the number of pixels in which the fractional polarisation is always below the distribution is two.

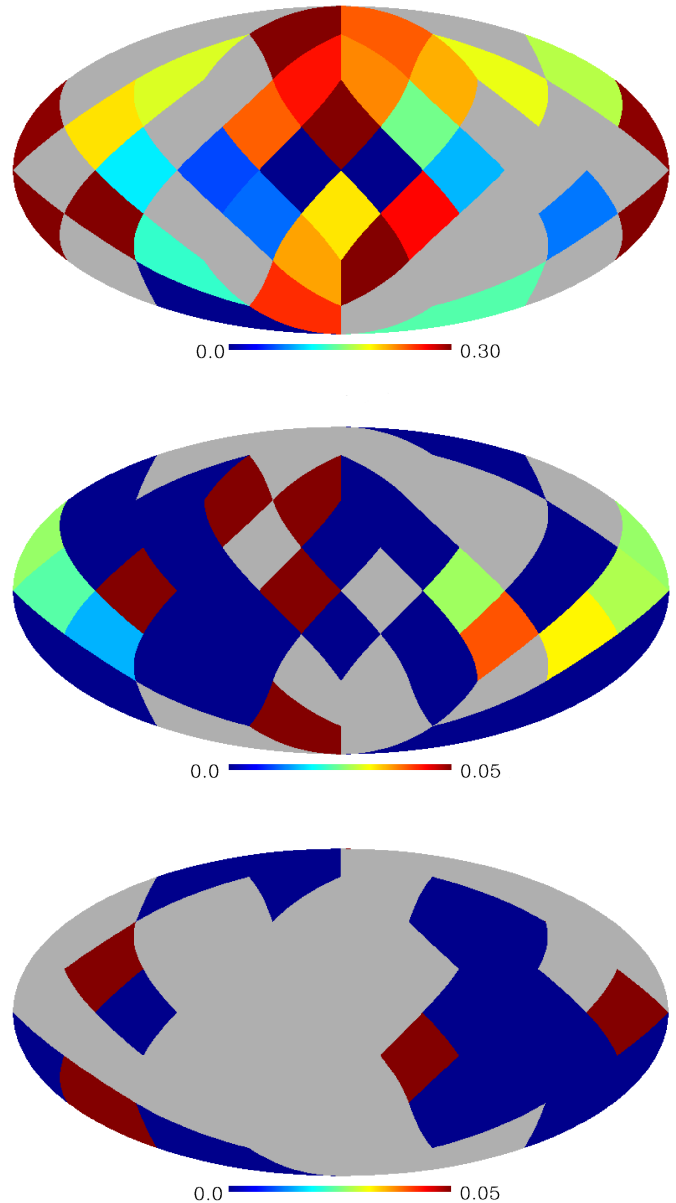


**Figure 4.** Synchrotron-correlated (*top*), dust-correlated (*middle*), and free-free-correlated (*bottom*) fractional polarisations in the 48 regions of the K-band pixel-analysis. The regions compatible with a zero polarisation fraction within  $1\sigma$  are plotted in blue. Regions with  $2\sigma_p > 30\%$ , or with negative fractional polarisation, are plotted in grey.

25, 27, 32, 34, 35, 45) the detections are at more than the  $2\sigma$  level. Some of these regions also show a (small) increase in synchrotron polarisation with respect to simulation results (e.g., 5, 17, 32), with an accompanying anti-correlation with the dust values. Indeed, in some cases, the recovered dust polarisation fraction becomes slightly negative, such as in region 5 (see Fig. 7), which is evidence of cross-talk between components. Six regions (5, 17, 23, 34, 35, and 45) out of the 48 exceed the simulated distributions at the 99th percentile and are individually significant at  $> 2\sigma$ . They showed fractional polarisations in the range 2.6–7.2 % except for the anomalous pixel 45, which appears to have a high polarisation fraction of  $32 \pm 12\%$ , detected at a significance level of  $2.7\sigma$ . This

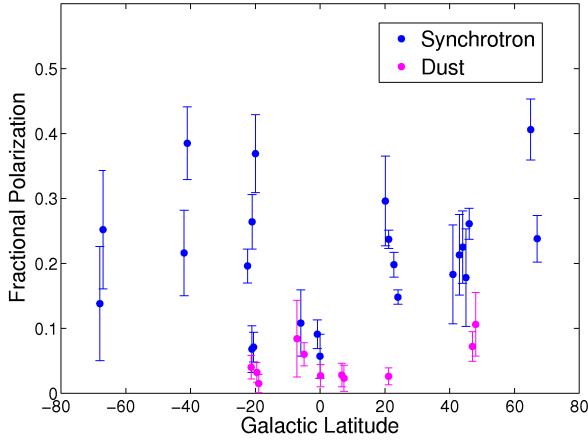


**Figure 5.** Synchrotron- and dust-correlated fractional polarisation of WMAP K-band as a function of mean Galactic latitude in the 48 regions of the pixel-analysis. We plot only regions where  $f_P > \sigma_{f_P}$ .

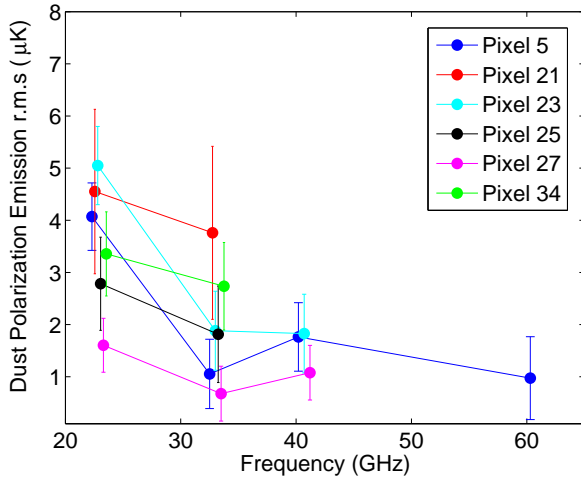


**Figure 6.** Dust-correlated polarised emission r.m.s. in  $\mu\text{K}$  as a function of frequency in the pixel-analysis. We report only the six pixel regions where there is a  $2\sigma$  significant emission in the K-band.

region does not contain any strong foreground features in total-intensity or in polarisation. Additionally, the simulation recovers the correct polarisation but with a relatively large uncertainty. The detected value in the real data is well outside the distribution, as shown in Fig. 8. This region should be investigated further with higher sensitivity data (e.g., WMAP 9-year, *Planck*).

Although we cannot rely heavily on individual pixels, we can still continue, knowing that there can be biases of up to  $\approx 5\%$  in any given region, and  $\approx 1.5\%$  when averaging significant ( $> 2\sigma$ ) pixels, as discussed in Section 5.1. Furthermore, we can choose pixels that in the simulations were able to recover the correct dust amplitude within  $1\sigma$  of the true value (regions 6, 12, 25, 33, 34, 35, 39, and 45). Although these may not be completely representative of the real data, they should be more reliable than simply averaging all or just significant pixels. For these, we find a weighted average of  $3.2 \pm 0.9$  (stat)  $\pm 1.5$  (sys) %. We do not claim this as a real detection, since this is only a  $\approx 2\sigma$  detection when considering the overall bias seen in the simulations described in Section 5.1. How-

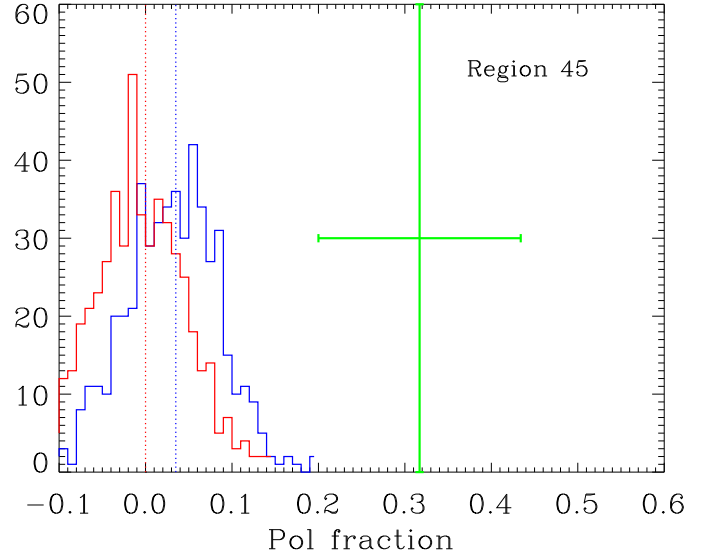


**Figure 8.** Histogram of the K-band dust polarisation fraction for region 45, from 500 realisations, for the case with no dust polarisation (red line) and with 3.5 % dust polarisation (blue line). The input values are shown as vertical dotted lines. The green line and error-bar represent the best-fitting value and its  $1\sigma$  uncertainty from the real data.

ever, it is clear that the average K-band dust polarisation fraction is less than about 5 % at 95 % confidence.

A comparison of the dust and synchrotron values at K-band (Fig. 5; as a function of Galactic latitude) shows that the K-band synchrotron polarisation increases from  $f_s \sim 5\%$  to  $\sim 40\%$ , while the dust remains fairly constant within the error-bars at  $f_d \sim 2\% - 10\%$  in the pixels where significant dust polarisation emission is found. Over most of the sky dust is found to be unpolarised, with a  $2\sigma$  upper limit on fractional polarisation of about 5% in seventeen pixel regions and about 10% in four other regions.

Given the limitations of our results, particularly at frequencies above 33 GHz, we cannot make a detailed analysis of the frequency dependence of the dust polarisation. Fig. 6 reports the r.m.s. of the dust polarisation emission. The fractional polarisation for these same data are plotted in Fig. 9 (pixel 21 has been removed from this plot as the temperature-analysis yields negative C-C coefficients). Here we report just K-, Ka-, and Q-bands, as the higher frequency data have signal-to-noise ratios less than  $1\sigma$ . While the fractional polarisation data do exhibit a slight frequency dependence the uncertainties are quite large. Due to these large uncertainties we provide only a broad discussion, rather than a detailed analysis, of these results in the remainder of this section.

In the all-sky analysis (Fig. 2) the total emission from the anomalous-dust component appears to dominate the thermal dust component for frequencies below 61 GHz (V-band). We find similar results in the temperature data of the five pixels of Fig. 9 (not shown). Lazarian & Draine (2000) predicted that spinning-dust polarisation should be no greater than 2% at 20 GHz and become almost completely unpolarised above 40 GHz. If the anomalous component is due to spinning-dust then the dust-correlated polarisation should be consistent with zero-polarisation in the frequency range 40–61 GHz (Q–V bands), with the possibility of increasing polarisation towards lower frequencies. Within the error-bars, this is at least consistent with the behaviour observed in Fig. 9. Alternatively, Draine & Lazarian (1999) predict polarisations as high as 40% in the 1–200 GHz range for emission from vibrating magnetic-grains

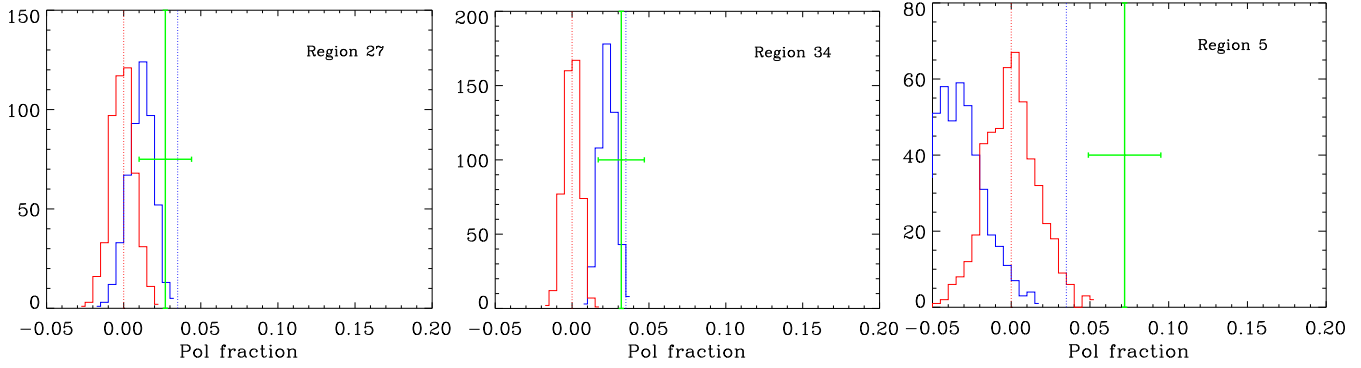


**Figure 7.** Histograms of the K-band dust polarisation fraction for three regions, from 500 realisations, for the case with no dust polarisation (red line) and with 3.5 % dust polarisation (blue line). The input values are shown as vertical dotted lines. The green line and error-bar represent the best-fitting value and its  $1\sigma$  uncertainty from the real data.

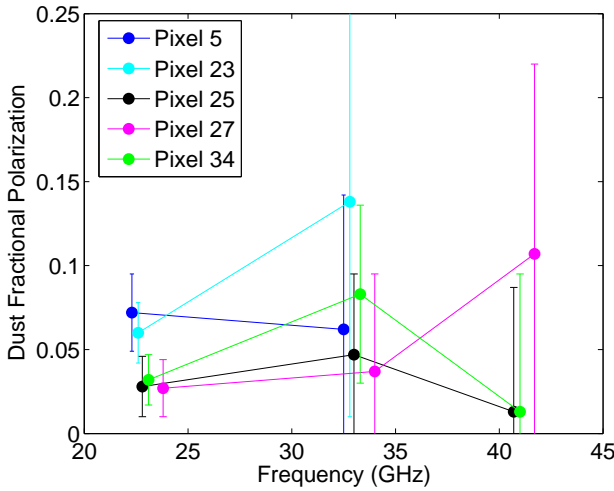


**Figure 9.** Dust-correlated polarisation fraction as a function of frequency in the pixel-analysis. We report only the five pixel regions where there is a  $> 1\sigma$  result in the K-band that also have a non-zero value at Ka and Q bands.

(although the actual polarisation is not expected to be so high given some level of beam depolarisation and depolarisation due to line-of-sight integration). Depending on the exact number of magnetic-domains and the grains' aspect ratios, the magnetic-grains' polarisation may drop from its maximal value to zero almost anywhere within the same frequency range; the observed polarisation as a function of frequency could have almost any behaviour (i.e., rising, falling, flat, or all three). Given the large uncertainties, we can only note here that the data plotted in Fig. 9 is not inconsistent with this behaviour.

### 5.5 Free Free

A simple fit to a power-law spectrum for the free-free emission in the all-sky analysis yields a free-free spectral index of  $\beta_f = -2.15 \pm 0.22$ . In the latitude analysis and in the all-sky analysis we find free-free emission is unpolarised ( $\lesssim 1\%$ ) over the sky. This result is confirmed in the pixel-analysis, where over most of the sky free-free is unpolarised at the  $1\sigma$  level, as reported in Table 3.

The upper limits in the distributions of the polarisation fraction from simulations in K-band typically range between 5 and 15

percent, apart from the regions around the Galactic poles that are essentially unconstrained. We find that in region 16 the detected free-free polarisation is higher than all simulation results but still compatible with zero at the  $2\sigma$  level when C-C errors are considered. In 16 of the 48 pixel regions we were able to put  $2\sigma$  upper limits on fractional polarisations ranging from 10% (in seven regions) to about 5% (in nine regions). These upper limits are more stringent where the uncertainties are small, i.e., where the free-free emission is higher, such as near the Galactic plane at longitudes between  $200^\circ$  and  $300^\circ$ . Some pixels (e.g., 14, 16, 17, 24, 31, 33, 40, and 43) do show significant cross-talk in the simulations. By comparing the simulations with the real data, we can isolate regions that we believe are not strongly affected by cross-talk and where the C-C errors are comparable or larger to the scatter in the simulations (therefore no significant bias). These are 4, 10, 11, 13, 15, 19, 22, 23, 26, 27, 32, 34, and 41. Examples are shown in Fig. 10. The weighted average of these more reliable pixels is  $0.0 \pm 1.7\%$ , corresponding to an upper limit of 3.4 % (95 % confidence). The standard deviation in all 48 pixels is  $\pm 5.5\%$ . We note that, unlike for dust, no regions exceed the simulation distributions at the 99th percentile and are individually significant (at  $> 2\sigma$ ).

## 6 CONCLUSIONS

We computed the cross-correlation of the intensity and polarisation WMAP data in different sky regions using templates for synchrotron, dust, and free-free emission, plus a monopole-offset template. This technique is reliable because it takes into account the correlations between foregrounds, and because it requires no assumptions about the foregrounds' frequency behaviours. However, this study relies on the assumption of equal polarisation angles for the three foregrounds and on the hypothesis of constant fractional polarisation fraction in each of the analysed sky-regions. We derive the frequency dependence and polarisation fraction for all three components in 48 different sky regions (delineated in HEALPix format at  $N_{\text{side}} = 2$  resolution).

This resolution is chosen as a compromise between (a) the assumption of uniform polarisation fraction in any given sky-region and (b) the need to average a large number of data points in order to minimise uncertainties.

The anomalous low-frequency emission correlated with thermal-dust is clearly detected in intensity over the entire sky at the WMAP K- and Ka- bands. It is also found to be the dominant foreground at low Galactic latitude in the pixel analysis, between

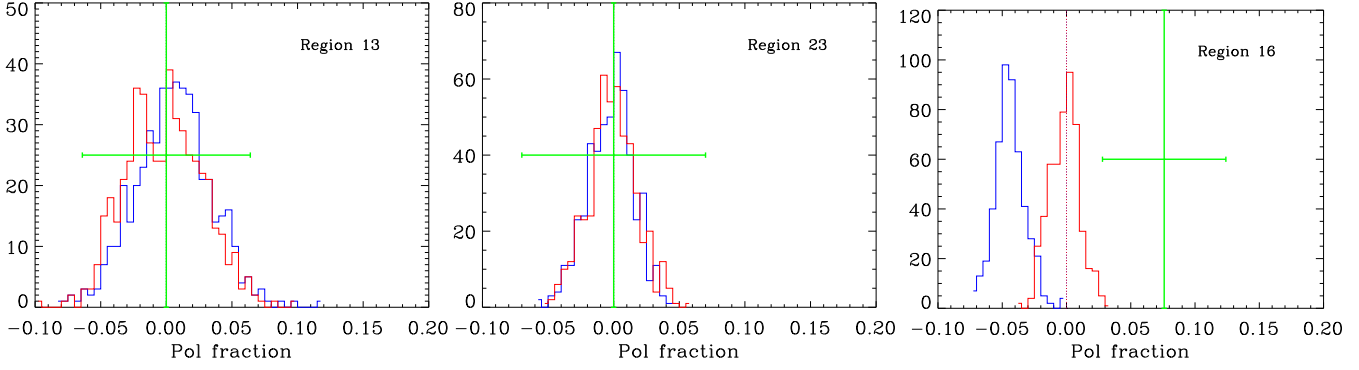


**Figure 10.** Histograms of the free-free polarisation fraction at K-band for three regions, from 500 realisations at K-band, for the case with no dust polarisation (red line) and with 3.5 % dust polarisation (blue line). The input values are shown as vertical dotted lines. The green line and error-bar represents the best-fitting value and its  $1\sigma$  uncertainty from the real data.

$b = -40^\circ$  and  $b = 10^\circ$ . The synchrotron spectral-index obtained from the K- and Ka-bands is consistent with previous results, although small differences are found between the polarisation and temperature results in the pixel-analysis. On the other hand, the values from the all-sky analysis ( $\beta = -3.32 \pm 0.12$  for intensity and  $\beta = -3.01 \pm 0.03$  from polarisation) are compatible with an average value of  $\beta \simeq -3$ .

The polarisation fraction of the synchrotron is constant in frequency and increases with latitude from 5% near the Galactic plane to about 40% in some regions at high latitude; this is consistent with a depolarisation effect due to integrating through high-column densities in the plane. The average synchrotron fractional polarisation at low latitude ( $|b| < 20^\circ$ ) is  $8.6 \pm 1.7$  (stat)  $\pm 0.5$  (sys) %, while at high latitude ( $|b| > 20^\circ$ ) is  $19.3 \pm 0.8$  (stat)  $\pm 0.5$  (sys) % with a standard deviation of  $\pm 11.0\%$ . The robustness of these values was verified using monte carlo simulations.

Previous work has usually assumed that the anomalous dust-correlated emission in K-band is unpolarised. We find this assumption to be reasonable with most of the sky having polarisation fractions less than 10%. However, monte carlo simulations revealed that some pixels are likely to be affected by cross-talk, at up to the  $\approx 5\%$  level. Taking an average of the significant ( $> 2\sigma$ ) regions led to a bias of  $\approx 1.5\%$  in the simulations. The average polarisation fraction, for the more reliable pixels, was  $3.2 \pm 0.9$  (stat)  $\pm 1.5$  (sys) %. Given the average bias seen in the simulations (1.5%), we do not claim a strong detection, while it is clear that the polarisation fraction is less than 5% at 95% confidence. We found several pixels that appeared to have a significant detection of dust polarisation at K-band while being robust in the simulations. Eight out of 48 regions exceeded the 99th percentile of the distribution from simulations with no input foreground polarisation, 6 of which are detected at above  $2\sigma$  and display polarisation fractions between 2.6% and 7.2%, except for region 45 at  $(l, b) \sim (46^\circ, -66^\circ)$ , which was found to be polarised at  $31.7 \pm 11.7\%$  ( $2.7\sigma$ ).

Free-free emission is found to be unpolarised over the entire sky with an upper limit on the fractional polarisation of about 5% in nine regions, and about 10% in seven regions. Unlike for the dust, no regions were found to have a polarisation fraction that exceeded the simulation distributions. Guided by simulations, we find an upper limit of 3.4% (95% confidence).

## ACKNOWLEDGMENTS

This research was carried out at the Jet Propulsion Laboratory, California Institute of Technology, under a contract with the National Aeronautics and Space Administration and funded through the Director's Research and Development Fund Program. EP is an NSF-ADVANCE fellow (AST 06-49899) also supported by NASA grant NNX07AH59G and Planck subcontract 1290790. NM and EP were supported by JPL SURP award 1314616 for this work, and would like to thank Caltech for hospitality during this period. EP wishes to thank the Aspen Center for Physics where part of this work was carried out. CD acknowledges an STFC Advanced Fellowship and ERC grant under the FP7. JEV is supported by NSF AST 05-40882 and 08-38261 through the Caltech Submillimeter Observatory. The authors would like to thank Mark Halpern and Anthony Banday for useful conversations. We acknowledge the use of the Legacy Archive for Microwave Background Data Analysis (LAMBDA). Support for LAMBDA is provided by the NASA Office of Space Science. Some of the results in this paper have been derived using the HEALPix (Górski et al., 2005) package.

## REFERENCES

- Ali-Haïmoud, Y., Hirata, C. M., & Dickinson, C. 2009, MNRAS, 395, 1055
- Banday A.J., Dickinson C., Davies R.D., Davis R.J., Górski K.M., 2003, MNRAS, 345, 897
- Battistelli E. S. et al. 2006, ApJ, 645, 141
- Bennett C.L. et al. 2003, ApJS, 148, 97
- Betoule, M., Pierpaoli, E., Delabrouille, J., Le Jeune, M., & Cardoso, J.-F. 2009, A&A, 503, 691
- Brown M.L. et al. 2009, ApJ, submitted (arXiv:0906.1003)
- Casassus, S., Cabrera, G. F., Förster, F., Pearson, T. J., Readhead, A. C. S., & Dickinson, C. 2006, ApJ, 639, 951
- Chiang H.C. et al. 2009, (arXiv:0906.1181)
- Cumberbatch, D. T., Zuntz, J., Kamfjord Eriksen, H. K., & Silk, J. 2009, (arXiv:0902.0039)
- de Oliveira-Costa A. et al. 1999, ApJ, 527, L9
- de Oliveira-Costa A. et al. 2002, ApJ, 567, 363
- Davies R.D., Watson R.A., Gutierrez C.M., 1996, MNRAS, 278, 925
- Davies R.D., Dickinson C., Banday A.J., Jaffe T.R., Górski K.M., Davis R.J., 2006, MNRAS, 370, 1125
- Delabrouille, J., & Cardoso, J.-F. 2009, Lecture Notes in Physics, Berlin Springer Verlag, 665, 159
- Dickinson C., Davies R.D., Davis R.J., 2003, MNRAS, 341, 369
- Dickinson, C., et al. 2004, MNRAS, 353, 732
- Dickinson, C., et al. 2009a, ApJ, 690, 1585



- Dickinson, C., et al. 2009b, *ApJ*, 705, 1607
- Dickinson, C., et al. 2010, *MNRAS*, 407, 2223
- Dotson J. L., Davidson J., Dowell C. D., Schleuning D. A., & Hildebrand R. H. 2000, *ApJS*, 128, 335
- Dotson J. L., Vaillancourt, J. E., Kirby, L., Dowell, C. D., Hildebrand, R. H., & Davidson, J. A., 2010, *ApJS*, 186, 406
- Draine B.T., Lazarian A., 1998a, *ApJ*, 494, L19
- Draine B.T., Lazarian A., 1998b, *ApJ*, 508, 157
- Draine B.T., Lazarian A., 1999, *ApJ*, 512, 740
- Dunkley, J., et al. 2009, *ApJ*, 701, 1804
- Eriksen H.K., Banday A.J., Górski K.M., Lilje, P.B., 2004, *ApJ*, 612, 633
- Eriksen, H. K., Jewell, J. B., Dickinson, C., Banday, A. J., Górski, K. M., & Lawrence, C. R. 2008, *ApJ*, 676, 10
- Finkbeiner D.P., 2003, *ApJS*, 146, 407
- Finkbeiner D.P., 2004, *ApJ*, 614, 186
- Finkbeiner D.P., Davis M., Schlegel D.J., 1999, *ApJ*, 524, 867
- Finkbeiner D.P., Langston G.I., Minter A.H., 2004, *ApJ*, 617, 350
- Fosalba P., Lazarian A., Prunet S., & Tauber J. A. 2002, *ApJ*, 564, 762
- Gold, B., et al. 2009, *ApJS*, 180, 265
- Górski, K. M. et al. 1996, *ApJL*, 464, L11
- Górski, K. M., Hivon, E., Banday, A. J., Wandelt, B. D., Hansen, F. K., Reinecke, M., & Bartelmann, M. 2005, *ApJ*, 622, 759
- Haslam C.G.T., Klein U., Salter C.J., Stoffel H., Wilson W.E., Cleary M.N., Cooke D.J., Thomasson P., 1981, *A&A*, 100, 209
- Haslam C.G.T., Stoffel H., Salter C.J., Wilson W.E., 1982, *A&AS*, 47, 1
- Heiles C. 2000, *AJ*, 119, 923
- Hildebrand R. & Kirby L. 2004, in *ASP Conf. Ser.* 309, *Astrophysics of Dust*, ed. A. N. Witt, G. C. Clayton, & B. T. Draine (San Francisco: ASP), 515
- Hildebrand R. H., Dotson J. L., Dowell C. D., Schleuning D. A., & Vaillancourt J. E. 1999, *ApJ*, 516, 834
- Hildebrand R. et al. 2007, *MNRAS*, 382, 594
- Hinshaw, G., et al. 2007, *ApJS*, 170, 288
- Hinshaw, G., et al. 2009, *ApJS*, 180, 225
- Jonas J.L., Baart E.E., Nicolson G.D., 1998, *MNRAS*, 297, 977
- Jones, W. C., et al. 2006, *ApJ*, 647, 823
- Kogut A. et al. 1996, *ApJ*, 464, L5
- Kogut A. et al. 2007, *ApJ*, 665, 355
- Lazarian A. 2003, *J. Quant. Spectros. Radiat. Transfer*, 79, 881
- Lazarian A. 2007, *J. Quant. Spectros. Radiat. Transfer*, 106, 225
- Lazarian A., Draine B.T., 2000, *ApJ*, 536, 15
- Lazarian, A., & Finkbeiner, D. 2003, *New Astronomy Review*, 47, 1107
- Leach, S. M. et al. 2008, *A&A*, 491, 597
- López-Caraballo, C. H., Rubiño-Martín, J. A., Rebolo, R., & Génova-Santos, R. 2011, *ApJ*, 729, 25
- Martin P. G., 2007, *EAS Publ. Ser.* 23: *Sky Polarisation at Far-Infrared to Radio Wavelengths: The Galactic Screen before the Cosmic Microwave Background*, 165
- Mason, B. S., Robshaw, T., Heiles, C., Finkbeiner, D., & Dickinson, C. 2009, *ApJ*, 697, 1187
- Mather, J. C., Fixsen, D. J., Shafer, R. A., Mosier, C., & Wilkinson, D. T. 1999, *ApJ*, 512, 511
- Matthews, B. C., McPhee, C., Fissel, L., & Curran, R. 2009, *ApJS*, 182, 143
- Miville-Deschênes, M. A. et al. 2008, *A&A*, 490, 1093
- Nolta M. et al. 2008, *ApJS*, 180, 246
- Page L. et al. 2007, *ApJS*, 170, 335
- Planck Collaboration, 2011, accepted in *A&A* (arXiv:1101.2031)
- Platania P. et al. 2003, *A&A*, 410, 847
- Ponthieu N. et al. 2005, *A&A*, 444, 327
- Pryke, C., et al. 2009, *ApJ*, 692, 1247
- Reich P., Reich W., 1986, *A&AS*, 63, 205
- Reich P., Reich W., 1988, *A&A*, 196, 211
- Reichardt C.L. et al. 2009, *ApJ*, 694, 1200
- Rybicki, G. B., & Lightman, A. P. 1979, *Radiative Processes in Astrophysics*, New York, Wiley-Interscience, 1979
- Scaife, A. M. M., et al. 2009, *MNRAS*, 400, 1394
- Schlegel D.J., Finkbeiner D.P., Davis M., 1998, *ApJ*, 500, 525
- Sievers J.L. et al. 2009, *ApJ*, submitted (arXiv:0901.4540)
- Simmons, J. F. L. & Stewart, B. G. 1985, *A&A*, 142, 100
- Vaillancourt J. E., 2006, *PASP*, 118, 1340
- Vaillancourt J. E., Dowell C. D., Hildebrand R. H., Kirby L., Krejny M. M., Li H.-b., Novak G., Houde M., Shinnaga H., & Attard M. 2008, *ApJ*, 679, L25
- Watson R.A., Rebolo R., Rubiño-Martín J.A., Hildebrandt S., Gutiérrez C.M., Fernández-Cerezo S., Hoyland R.J., Battistelli E.S., 2005, *ApJ*, 624, L89
- Wolleben, M., Landecker, T. L., Reich, W., & Wielebinski, R. 2006, *A&A*, 448, 411

## APPENDIX A: COMPLETE TABLES OF CROSS-CORRELATION COEFFICIENTS

Here we report the C-C coefficients for dust, synchrotron and free-free resulting from our analysis.



Pixel	K-band	Ka-band	Q-band	V-band	W-band
Dust Temperature C-C coefficients					
1	12.8 $\pm$ 2.7	9.2 $\pm$ 2.9	8.4 $\pm$ 3.2	7.6 $\pm$ 2.8	7.2 $\pm$ 3.8
2	-2.9 $\pm$ 5.2	-10.4 $\pm$ 5.6	-10.7 $\pm$ 6	-11.5 $\pm$ 5.9	-10 $\pm$ 6.8
3	8.2 $\pm$ 2.8	2.7 $\pm$ 2.8	0.7 $\pm$ 2.8	0.8 $\pm$ 3.2	0.3 $\pm$ 3.4
4	6.9 $\pm$ 2.5	1.6 $\pm$ 2.5	-0.4 $\pm$ 2.6	-0.6 $\pm$ 2.7	0.6 $\pm$ 3.4
5	8.2 $\pm$ 0.6	2.4 $\pm$ 0.7	1.1 $\pm$ 0.7	0.7 $\pm$ 0.7	1 $\pm$ 0.7
6	15.4 $\pm$ 2.5	8.5 $\pm$ 2.7	6.5 $\pm$ 2.6	5.7 $\pm$ 2.7	4.8 $\pm$ 3
7	5 $\pm$ 0.5	1.7 $\pm$ 0.5	1 $\pm$ 0.5	0.8 $\pm$ 0.7	1.1 $\pm$ 0.6
8	8.4 $\pm$ 1.2	4.1 $\pm$ 1.3	2.9 $\pm$ 1.4	2.4 $\pm$ 1.3	2.3 $\pm$ 1.4
9	3.1 $\pm$ 3	-0.6 $\pm$ 3.1	-1.9 $\pm$ 3.2	-2.2 $\pm$ 3.5	-1.6 $\pm$ 3.4
10	7.8 $\pm$ 1.7	2.8 $\pm$ 1.8	1.4 $\pm$ 2	1.1 $\pm$ 2.1	0.7 $\pm$ 2
11	8.3 $\pm$ 1.2	3 $\pm$ 1.2	2 $\pm$ 1.3	1.7 $\pm$ 1.3	1.7 $\pm$ 1.3
12	9.5 $\pm$ 0.9	1.9 $\pm$ 1	0.2 $\pm$ 0.9	-1 $\pm$ 1.1	-0.5 $\pm$ 1.3
13	8.3 $\pm$ 0.6	3.2 $\pm$ 0.6	2.2 $\pm$ 0.7	1.5 $\pm$ 0.7	1.7 $\pm$ 0.7
14	5.3 $\pm$ 0.4	1.5 $\pm$ 0.5	0.6 $\pm$ 0.5	0.3 $\pm$ 0.5	0.7 $\pm$ 0.5
15	6.8 $\pm$ 0.2	2.3 $\pm$ 0.2	1.3 $\pm$ 0.2	0.8 $\pm$ 0.3	1.1 $\pm$ 0.2
16	4.8 $\pm$ 0.3	0.7 $\pm$ 0.3	-0.2 $\pm$ 0.3	-0.6 $\pm$ 0.3	-0.2 $\pm$ 0.4
17	7.3 $\pm$ 0.3	3.3 $\pm$ 0.3	2.2 $\pm$ 0.3	1.6 $\pm$ 0.3	1.9 $\pm$ 0.4
18	9.5 $\pm$ 0.7	5.5 $\pm$ 0.7	4.7 $\pm$ 0.7	4 $\pm$ 0.7	4.1 $\pm$ 0.7
19	3.7 $\pm$ 0.6	-0.1 $\pm$ 0.6	-0.7 $\pm$ 0.6	-0.9 $\pm$ 0.7	-0.1 $\pm$ 0.6
20	8 $\pm$ 0.8	2.1 $\pm$ 0.9	0.9 $\pm$ 0.9	0.4 $\pm$ 0.9	0.7 $\pm$ 1.1
21	5.2 $\pm$ 0.7	0.6 $\pm$ 0.8	-0.4 $\pm$ 0.8	-0.7 $\pm$ 0.7	-0.7 $\pm$ 0.8
22	4.3 $\pm$ 0.4	0.6 $\pm$ 0.4	-0.1 $\pm$ 0.4	-0.4 $\pm$ 0.5	0.1 $\pm$ 0.4
23	5.3 $\pm$ 0.4	0.9 $\pm$ 0.4	-0.2 $\pm$ 0.4	-0.7 $\pm$ 0.5	-0.3 $\pm$ 0.5
24	6.5 $\pm$ 0.4	2.7 $\pm$ 0.4	1.8 $\pm$ 0.4	1.4 $\pm$ 0.4	1.9 $\pm$ 0.5
25	5.9 $\pm$ 0.3	2.3 $\pm$ 0.3	1.4 $\pm$ 0.4	0.9 $\pm$ 0.3	1.3 $\pm$ 0.4
26	5.9 $\pm$ 0.6	0.9 $\pm$ 0.6	-0.2 $\pm$ 0.7	-0.7 $\pm$ 0.7	-0.2 $\pm$ 0.8
27	5.6 $\pm$ 0.4	1.7 $\pm$ 0.4	0.9 $\pm$ 0.4	0.5 $\pm$ 0.5	1 $\pm$ 0.5
28	9 $\pm$ 4.1	0.9 $\pm$ 4.2	0.4 $\pm$ 4.8	-1.3 $\pm$ 4.9	0.2 $\pm$ 5.2
29	11.5 $\pm$ 0.6	4.9 $\pm$ 0.6	3.5 $\pm$ 0.7	2.4 $\pm$ 0.8	2.5 $\pm$ 0.8
30	8.3 $\pm$ 0.6	3.3 $\pm$ 0.6	2.1 $\pm$ 0.7	1.4 $\pm$ 0.6	1.8 $\pm$ 0.6
31	11.8 $\pm$ 0.5	6.5 $\pm$ 0.5	5 $\pm$ 0.6	4 $\pm$ 0.6	3.8 $\pm$ 0.6
32	7.7 $\pm$ 0.4	2.7 $\pm$ 0.4	1.5 $\pm$ 0.4	0.8 $\pm$ 0.5	1.2 $\pm$ 0.5
33	6.1 $\pm$ 0.2	2.8 $\pm$ 0.2	1.9 $\pm$ 0.2	1.5 $\pm$ 0.2	1.7 $\pm$ 0.2
34	4.9 $\pm$ 0.2	1.5 $\pm$ 0.3	0.9 $\pm$ 0.3	0.7 $\pm$ 0.3	1.1 $\pm$ 0.3
35	5.9 $\pm$ 0.6	1.5 $\pm$ 0.6	0.4 $\pm$ 0.7	-0.1 $\pm$ 0.6	0.3 $\pm$ 0.8
36	7.1 $\pm$ 0.3	2.8 $\pm$ 0.3	1.7 $\pm$ 0.4	1.1 $\pm$ 0.4	1.3 $\pm$ 0.4
37	4.4 $\pm$ 1.4	-0.5 $\pm$ 1.5	-1.3 $\pm$ 1.7	-2.1 $\pm$ 1.4	-1.7 $\pm$ 1.6
38	8.3 $\pm$ 1	3.3 $\pm$ 1	2.1 $\pm$ 1.1	1.1 $\pm$ 1.1	1.4 $\pm$ 1.3
39	5.4 $\pm$ 0.8	0.7 $\pm$ 0.8	0 $\pm$ 0.9	-0.6 $\pm$ 1	-0.1 $\pm$ 0.9
40	7 $\pm$ 0.3	2.1 $\pm$ 0.3	0.8 $\pm$ 0.3	0 $\pm$ 0.3	0.2 $\pm$ 0.4
41	8.7 $\pm$ 0.5	3.1 $\pm$ 0.5	1.8 $\pm$ 0.5	1 $\pm$ 0.5	1.3 $\pm$ 0.5
42	7.3 $\pm$ 2.3	3.8 $\pm$ 2.5	2.7 $\pm$ 2.6	2.4 $\pm$ 2.6	2.5 $\pm$ 2.4
43	9 $\pm$ 0.6	4.2 $\pm$ 0.6	2.9 $\pm$ 0.7	1.9 $\pm$ 0.6	2.1 $\pm$ 0.6
44	6 $\pm$ 2	0.9 $\pm$ 2	0.4 $\pm$ 2.3	-0.5 $\pm$ 2.5	0.3 $\pm$ 2.7
45	8.5 $\pm$ 2.3	4.3 $\pm$ 2.5	1.9 $\pm$ 2.6	1.9 $\pm$ 2.7	1.4 $\pm$ 3.2
46	1.2 $\pm$ 1.2	-3.4 $\pm$ 1.3	-4.4 $\pm$ 1.3	-4.4 $\pm$ 1.2	-3.3 $\pm$ 1.5
47	16.2 $\pm$ 3.2	8.8 $\pm$ 3.2	6.6 $\pm$ 3.6	6.3 $\pm$ 3.9	5.9 $\pm$ 3.9
48	3.3 $\pm$ 5.5	-1.8 $\pm$ 5.9	-3.1 $\pm$ 6.2	-5.7 $\pm$ 6.6	-5.4 $\pm$ 5.9

**Table A1.** Full fit temperature coefficients for dust in all 48 pixel regions, with associated 1- $\sigma$  errors (in  $\mu K \mu K_{FDS}^{-1}$ ).

Pixel	K-band	Ka-band	Q-band	V-band	W-band
Dust Polarization C-C coefficients					
1	-1.1 $\pm$ 0.7	-0.4 $\pm$ 0.7	0.3 $\pm$ 0.6	-0.3 $\pm$ 0.8	-0.9 $\pm$ 1
2	-1.2 $\pm$ 1.5	0.1 $\pm$ 1.5	-0.3 $\pm$ 1.4	-0.3 $\pm$ 1.7	0.3 $\pm$ 2.1
3	0.4 $\pm$ 0.8	0.3 $\pm$ 0.8	0.2 $\pm$ 0.8	-0.6 $\pm$ 1	0.1 $\pm$ 1.1
4	-0.9 $\pm$ 0.8	0.2 $\pm$ 0.8	-0.2 $\pm$ 0.9	-0.4 $\pm$ 1	0.4 $\pm$ 1.2
5	0.6 $\pm$ 0.2	0.2 $\pm$ 0.2	0.3 $\pm$ 0.2	0.1 $\pm$ 0.2	0 $\pm$ 0.3
6	1.6 $\pm$ 0.7	0 $\pm$ 0.7	0.4 $\pm$ 0.6	-0.1 $\pm$ 0.8	-0.4 $\pm$ 1
7	-0.1 $\pm$ 0.1	0.1 $\pm$ 0.1	0 $\pm$ 0.1	0 $\pm$ 0.2	0 $\pm$ 0.2
8	-0.5 $\pm$ 0.3	-0.2 $\pm$ 0.3	0 $\pm$ 0.3	0.2 $\pm$ 0.4	0 $\pm$ 0.4
9	0 $\pm$ 0.9	0.1 $\pm$ 0.9	0.1 $\pm$ 0.8	0.3 $\pm$ 1	-0.2 $\pm$ 1.2
10	-0.3 $\pm$ 0.5	-0.2 $\pm$ 0.5	0.1 $\pm$ 0.5	0.4 $\pm$ 0.6	0.8 $\pm$ 0.7
11	-1.3 $\pm$ 0.4	0 $\pm$ 0.4	-0.1 $\pm$ 0.4	-0.1 $\pm$ 0.5	-0.3 $\pm$ 0.6
12	-0.4 $\pm$ 0.3	-0.3 $\pm$ 0.3	0 $\pm$ 0.3	0.1 $\pm$ 0.3	0.2 $\pm$ 0.4
13	-0.1 $\pm$ 0.2	0.3 $\pm$ 0.2	0 $\pm$ 0.2	0 $\pm$ 0.3	-0.1 $\pm$ 0.3
14	-1.6 $\pm$ 0.1	-0.4 $\pm$ 0.1	-0.2 $\pm$ 0.1	-0.1 $\pm$ 0.1	0 $\pm$ 0.1
15	-0.1 $\pm$ 0	0 $\pm$ 0	0 $\pm$ 0	0 $\pm$ 0	0 $\pm$ 0.1
16	-0.3 $\pm$ 0.1	0 $\pm$ 0.1	0 $\pm$ 0.1	0 $\pm$ 0.1	0 $\pm$ 0.1
17	0.2 $\pm$ 0.1	0 $\pm$ 0.1	0.1 $\pm$ 0.1	0 $\pm$ 0.1	-0.1 $\pm$ 0.1
18	-0.2 $\pm$ 0.2	0 $\pm$ 0.2	-0.1 $\pm$ 0.2	0 $\pm$ 0.2	-0.3 $\pm$ 0.3
19	-0.3 $\pm$ 0.2	0.1 $\pm$ 0.2	-0.1 $\pm$ 0.2	0 $\pm$ 0.2	0.2 $\pm$ 0.2
20	-0.1 $\pm$ 0.3	-0.2 $\pm$ 0.3	0.1 $\pm$ 0.3	-0.1 $\pm$ 0.4	0.2 $\pm$ 0.4
21	0.4 $\pm$ 0.3	0.4 $\pm$ 0.3	0.1 $\pm$ 0.3	0.1 $\pm$ 0.4	-0.2 $\pm$ 0.5
22	0 $\pm$ 0.1	0 $\pm$ 0.1	0 $\pm$ 0.1	0 $\pm$ 0.1	0 $\pm$ 0.2
23	0.3 $\pm$ 0.1	0.1 $\pm$ 0.1	0.1 $\pm$ 0.1	0 $\pm$ 0.1	-0.1 $\pm$ 0.2
24	0.2 $\pm$ 0.1	0.2 $\pm$ 0.1	0.1 $\pm$ 0.1	0.2 $\pm$ 0.2	-0.3 $\pm$ 0.2
25	0.2 $\pm$ 0.1	0.1 $\pm$ 0.1	0 $\pm$ 0.1	0 $\pm$ 0.1	0 $\pm$ 0.2
26	-0.1 $\pm$ 0.2	-0.1 $\pm$ 0.2	0 $\pm$ 0.2	0 $\pm$ 0.2	0 $\pm$ 0.2
27	0.2 $\pm$ 0.1	0.1 $\pm$ 0.1	0.1 $\pm$ 0.1	0 $\pm$ 0.1	0.1 $\pm$ 0.1
28	-0.8 $\pm$ 1.8	0.4 $\pm$ 1.9	-1.6 $\pm$ 1.8	-0.1 $\pm$ 2.2	-1.9 $\pm$ 2.6
29	-0.8 $\pm$ 0.2	-0.2 $\pm$ 0.2	-0.1 $\pm$ 0.2	-0.1 $\pm$ 0.2	0 $\pm$ 0.2
30	-0.2 $\pm$ 0.2	-0.1 $\pm$ 0.2	0.1 $\pm$ 0.2	0 $\pm$ 0.2	0 $\pm$ 0.3
31	0 $\pm$ 0.1	0 $\pm$ 0.1	0.1 $\pm$ 0.1	0 $\pm$ 0.1	0 $\pm$ 0.2
32	0.1 $\pm$ 0.1	-0.1 $\pm$ 0.1	0 $\pm$ 0.1	0.1 $\pm$ 0.1	0 $\pm$ 0.2
33	-0.1 $\pm$ 0.1	0 $\pm$ 0.1	0.1 $\pm$ 0.1	0 $\pm$ 0.1	0 $\pm$ 0.1
34	0.2 $\pm$ 0.1	0.1 $\pm$ 0.1	0 $\pm$ 0.1	0 $\pm$ 0.1	0 $\pm$ 0.1
35	0.2 $\pm$ 0.1	0 $\pm$ 0.1	0 $\pm$ 0.1	0.1 $\pm$ 0.1	-0.1 $\pm$ 0.1
36	-0.1 $\pm$ 0.1	0 $\pm$ 0.1	0.1 $\pm$ 0.1	0 $\pm$ 0.1	0 $\pm$ 0.1
37	-0.7 $\pm$ 0.4	-0.2 $\pm$ 0.4	-0.4 $\pm$ 0.4	0.1 $\pm$ 0.5	0.1 $\pm$ 0.6
38	0.1 $\pm$ 0.3	-0.1 $\pm$ 0.3	0.1 $\pm$ 0.3	0 $\pm$ 0.3	0.1 $\pm$ 0.4
39	0.2 $\pm$ 0.3	-0.1 $\pm$ 0.3	-0.1 $\pm$ 0.3	-0.1 $\pm$ 0.3	0 $\pm$ 0.4
40	0 $\pm$ 0.1	0 $\pm$ 0.1	0 $\pm$ 0.1	0 $\pm$ 0.1	0 $\pm$ 0.1
41	0 $\pm$ 0.2	0 $\pm$ 0.2	0.1 $\pm$ 0.2	0 $\pm$ 0.2	0.2 $\pm$ 0.2
42	-1.1 $\pm$ 0.7	-0.2 $\pm$ 0.7	0.1 $\pm$ 0.6	0 $\pm$ 0.8	0.1 $\pm$ 1
43	0 $\pm$ 0.1	-0.1 $\pm$ 0.1	0 $\pm$ 0.1	0 $\pm$ 0.1	0 $\pm$ 0.1
44	-0.9 $\pm$ 0.5	-0.2 $\pm$ 0.5	-0.5 $\pm$ 0.5	0.2 $\pm$ 0.6	0.1 $\pm$ 0.8
45	2.7 $\pm$ 0.7	0 $\pm$ 0.7	0.4 $\pm$ 0.7	0 $\pm$ 0.9	0.1 $\pm$ 1
46	0.5 $\pm$ 0.3	0 $\pm$ 0.3	0.2 $\pm$ 0.3	0.2 $\pm$ 0.4	0 $\pm$ 0.5
47	-0.8 $\pm$ 0.8	-0.2 $\pm$ 0.8	-0.1 $\pm$ 0.7	0.2 $\pm$ 0.9	-0.5 $\pm$ 1.1
48	-0.7 $\pm$ 1.4	-0.5 $\pm$ 1.5	-0.9 $\pm$ 1.3	1 $\pm$ 1.7	-1.3 $\pm$ 2

**Table A2.** Full fit coefficients for polarized dust in all 48 pixel regions, with associated 1- $\sigma$  errors (in  $\mu K \mu K_{FDS}^{-1}$ ).

Pixel	K-band	Ka-band	Q-band	V-band	W-band
Synchrotron Temperature C-C coefficients					
1	5.9 ±0.6	2.1 ±0.6	1.3 ±0.7	0.5 ±0.7	0.4 ±0.6
2	-4.4 ±2	-6.9 ±2.2	-7 ±2.2	-6.8 ±2.4	-6.2 ±2.2
3	4.2 ±2.5	1.4 ±2.6	-0.1 ±2.8	-0.5 ±3.2	-0.3 ±3.4
4	8.4 ±0.9	4.4 ±0.9	3.4 ±0.9	2.8 ±1	1.9 ±1.3
5	6 ±0.4	3 ±0.4	2.3 ±0.4	1.9 ±0.4	1.5 ±0.5
6	0.6 ±1.4	-1.2 ±1.6	-1.7 ±1.5	-2 ±1.8	-1.7 ±1.9
7	4.8 ±1.2	2 ±1.3	1.5 ±1.5	0.6 ±1.6	0.7 ±1.6
8	2.3 ±1	-1.9 ±1.1	-2.8 ±1.2	-3.1 ±1.2	-3 ±1
9	4.2 ±1.8	0.5 ±1.9	-0.1 ±2	-0.5 ±2	-0.9 ±2.4
10	6.5 ±1.7	3.4 ±1.8	2.1 ±1.8	1.4 ±1.9	1.2 ±1.8
11	5.4 ±1	1.5 ±1	0.2 ±1	-0.1 ±1.2	-0.4 ±1
12	5.9 ±1	2.9 ±1	2 ±1	1.5 ±1.2	1 ±1.3
13	5.1 ±1.1	0.2 ±1.1	-1.1 ±1.2	-1.6 ±1.1	-1.5 ±1.3
14	7.2 ±0.3	3.4 ±0.3	2.5 ±0.3	1.9 ±0.4	1.4 ±0.4
15	-1.6 ±0.9	-4.2 ±0.9	-4.7 ±1	-4.9 ±1.1	-4.2 ±1.1
16	12.9 ±0.8	7.9 ±0.9	6.9 ±0.9	5.8 ±0.9	5.1 ±1.2
17	5.5 ±0.9	2.3 ±1	1.7 ±1.1	1.4 ±1.2	0.8 ±1
18	1.2 ±1.4	-1.2 ±1.4	-1.7 ±1.4	-1.8 ±1.4	-1.9 ±1.6
19	3 ±1.1	-0.9 ±1.1	-1.5 ±1.2	-1.8 ±1.4	-1.7 ±1.2
20	9.1 ±0.3	3.9 ±0.3	2.6 ±0.3	1.6 ±0.3	1.1 ±0.4
21	7 ±0.7	3.1 ±0.7	2.2 ±0.8	1.1 ±0.8	1.1 ±1
22	8.3 ±1.2	6 ±1.2	5.1 ±1.3	4.3 ±1.2	3.5 ±1.4
23	9.9 ±1.6	5.3 ±1.7	3.8 ±1.8	3.1 ±1.9	2.4 ±2.3
24	3.8 ±1.8	1.8 ±2	1.8 ±2.2	1.3 ±1.9	0.3 ±2.5
25	-3.7 ±0.9	-7.6 ±0.9	-8.6 ±0.9	-8.9 ±1.1	-7.8 ±1.2
26	2.6 ±1.7	3.1 ±1.9	3.4 ±1.9	3.4 ±2	3.4 ±2.4
27	10.4 ±0.8	6.1 ±0.9	5 ±0.9	3.8 ±0.9	2.9 ±1
28	11.3 ±2.2	6.9 ±2.4	5.1 ±2.6	4.1 ±2.6	3 ±2.6
29	7.2 ±0.6	1.7 ±0.6	0.3 ±0.7	-0.7 ±0.7	-0.6 ±0.7
30	4.2 ±0.6	0.9 ±0.6	0.2 ±0.7	-0.2 ±0.6	-0.3 ±0.7
31	-0.6 ±1.1	-3.5 ±1.2	-3.8 ±1.3	-4 ±1.2	-3.9 ±1.3
32	7.2 ±1	3.9 ±1.1	3 ±1.1	2.3 ±1.3	1.7 ±1.3
33	4.6 ±0.9	0.4 ±0.9	-0.4 ±0.9	-1 ±0.9	-1.3 ±1
34	14.6 ±1.3	10.2 ±1.3	8.7 ±1.4	7.1 ±1.6	6 ±1.7
35	0 ±1.6	-2.7 ±1.7	-3.1 ±1.6	-3 ±2	-2.8 ±1.8
36	4.4 ±0.5	-0.1 ±0.5	-1.2 ±0.6	-1.9 ±0.7	-1.8 ±0.6
37	7.1 ±1.3	3.1 ±1.4	1.9 ±1.3	2 ±1.3	1.1 ±1.4
38	-1.2 ±1.1	-3.4 ±1.1	-3.4 ±1.2	-3.5 ±1.1	-3 ±1.1
39	5.8 ±2	2 ±2.1	0.7 ±2.2	-0.4 ±2.3	0.3 ±2.8
40	-6.6 ±1.2	-10.7 ±1.3	-11.3 ±1.3	-11.3 ±1.3	-9.5 ±1.5
41	-3 ±1.5	-5 ±1.5	-5.8 ±1.7	-6.1 ±1.6	-5.4 ±1.8
42	2.4 ±2.2	-0.3 ±2.3	-1 ±2.2	-1.4 ±2.7	-1.5 ±2.9
43	-0.1 ±1.3	-2.3 ±1.4	-2.9 ±1.5	-3.2 ±1.4	-2.6 ±1.8
44	7.7 ±1	2.9 ±1	1.3 ±1	0.6 ±1.1	0.4 ±1.1
45	6.1 ±1.5	3.1 ±1.5	2.6 ±1.5	2.2 ±1.8	2 ±1.6
46	12.7 ±1.8	8.9 ±1.8	8 ±2.1	7.7 ±2	6.1 ±1.9
47	5.6 ±2	0.1 ±2.1	-0.9 ±2.4	-2 ±2.2	-1.8 ±2.7
48	-1.4 ±1.8	-4 ±2	-4.4 ±1.9	-4.8 ±2.2	-3.9 ±2.4

**Table A3.** Full fit temperature coefficients for Synchrotron in all 48 pixel regions, with associated 1- $\sigma$  errors (in  $\mu K K_{408MHz}^{-1}$ ).

Pixel	K-band	Ka-band	Q-band	V-band	W-band
Synchrotron Polarization C-C coefficients					
1	2.4 ±0.2	0.8 ±0.2	0.4 ±0.1	0 ±0.2	0.3 ±0.2
2	0.6 ±0.4	0.2 ±0.4	0.2 ±0.4	0 ±0.5	-0.4 ±0.6
3	1.9 ±0.7	0.4 ±0.7	0.3 ±0.7	0.7 ±0.8	0.2 ±1
4	2 ±0.2	0.6 ±0.2	0.2 ±0.2	-0.1 ±0.3	-0.2 ±0.3
5	1.6 ±0.1	0.5 ±0.1	0.3 ±0.1	0.1 ±0.1	0.1 ±0.1
6	0.5 ±0.3	0.4 ±0.3	0 ±0.3	0 ±0.3	0.1 ±0.4
7	0.9 ±0.3	0.2 ±0.3	-0.1 ±0.3	0 ±0.3	0.2 ±0.4
8	1 ±0.2	0.2 ±0.2	0 ±0.2	-0.1 ±0.3	0.1 ±0.3
9	0.7 ±0.5	0.5 ±0.5	0.3 ±0.5	0.1 ±0.6	0.3 ±0.8
10	1.2 ±0.4	0 ±0.4	0 ±0.4	0 ±0.4	0 ±0.5
11	1.2 ±0.3	0 ±0.3	-0.1 ±0.3	0.2 ±0.3	0.2 ±0.4
12	1.3 ±0.3	0.6 ±0.3	0.2 ±0.3	0.1 ±0.3	0.1 ±0.4
13	2.3 ±0.4	0.7 ±0.4	-0.1 ±0.4	-0.3 ±0.5	0.3 ±0.6
14	1.7 ±0.1	0.5 ±0.1	0.3 ±0.1	0.1 ±0.1	0 ±0.1
15	1.8 ±0.2	0.6 ±0.2	0.2 ±0.1	0 ±0.2	-0.1 ±0.2
16	2.6 ±0.2	0.7 ±0.2	0.3 ±0.2	0.1 ±0.2	0.2 ±0.3
17	1.6 ±0.3	0.5 ±0.3	-0.1 ±0.3	0 ±0.3	0.1 ±0.4
18	1 ±0.3	0 ±0.3	0.4 ±0.3	0 ±0.4	0.3 ±0.5
19	1.1 ±0.3	0.2 ±0.3	0.2 ±0.3	0 ±0.4	-0.1 ±0.4
20	1.3 ±0.1	0.3 ±0.1	0.1 ±0.1	0 ±0.1	0 ±0.1
21	-0.1 ±0.3	0.1 ±0.3	0 ±0.3	0 ±0.4	0.4 ±0.5
22	0.5 ±0.3	0 ±0.3	-0.1 ±0.2	0 ±0.3	-0.1 ±0.4
23	1.1 ±0.5	0.3 ±0.5	0.1 ±0.5	0.3 ±0.6	0.3 ±0.8
24	1.7 ±0.6	0.2 ±0.6	0.4 ±0.6	-0.6 ±0.8	0.8 ±0.9
25	1.5 ±0.3	0.1 ±0.3	0.2 ±0.3	0.3 ±0.3	0 ±0.4
26	0.6 ±0.4	0.3 ±0.4	0.1 ±0.4	0.1 ±0.5	0.1 ±0.6
27	1 ±0.2	0.2 ±0.2	-0.1 ±0.2	-0.1 ±0.3	0 ±0.3
28	0.5 ±1.1	-0.2 ±1.1	1 ±1	0.2 ±1.3	1 ±1.5
29	1.4 ±0.2	0.5 ±0.2	0.2 ±0.2	0 ±0.2	0 ±0.2
30	0.3 ±0.1	0.1 ±0.2	0 ±0.2	0 ±0.2	0 ±0.2
31	1.3 ±0.2	0.3 ±0.2	0.1 ±0.2	-0.1 ±0.3	0.1 ±0.3
32	2.6 ±0.2	1 ±0.2	0.4 ±0.2	-0.1 ±0.3	-0.2 ±0.3
33	2.5 ±0.3	0.8 ±0.3	0.2 ±0.3	0.2 ±0.4	-0.4 ±0.5
34	1 ±0.3	-0.1 ±0.3	0.1 ±0.3	-0.1 ±0.4	-0.1 ±0.5
35	0.6 ±0.3	0.3 ±0.3	0 ±0.3	-0.2 ±0.4	0.5 ±0.5
36	1.2 ±0.1	0.4 ±0.1	0.2 ±0.1	0.1 ±0.1	-0.1 ±0.2
37	1.5 ±0.4	0.3 ±0.4	0.3 ±0.4	-0.1 ±0.4	-0.3 ±0.5
38	0.5 ±0.3	0.6 ±0.3	0 ±0.3	-0.1 ±0.4	0 ±0.4
39	0.7 ±0.6	0.3 ±0.7	0.1 ±0.6	0.1 ±0.8	-0.1 ±0.9
40	0.5 ±0.3	0.3 ±0.3	0.1 ±0.3	0 ±0.3	0 ±0.4
41	0.3 ±0.4	0.1 ±0.4	-0.1 ±0.4	0 ±0.5	-0.2 ±0.6
42	1.8 ±0.5	0.4 ±0.5	0.3 ±0.4	0.1 ±0.6	0.1 ±0.7
43	1 ±0.2	0.5 ±0.2	0.1 ±0.2	-0.1 ±0.2	-0.1 ±0.3
44	3 ±0.2	0.9 ±0.2	0.6 ±0.2	-0.1 ±0.3	0 ±0.3
45	1.5 ±0.4	0.9 ±0.4	0 ±0.4	0 ±0.5	0.1 ±0.6
46	0.1 ±0.5	0 ±0.5	0.2 ±0.5	-0.1 ±0.6	-0.6 ±0.7
47	0.8 ±0.4	0.4 ±0.4	0.7 ±0.4	0.2 ±0.5	-0.1 ±0.6
48	2 ±0.4	0.7 ±0.4	0.4 ±0.3	-0.2 ±0.4	0 ±0.5

**Table A4.** Full fit coefficients for polarized synchrotron in all 48 pixel regions, with associated 1- $\sigma$  errors (in  $\mu K K_{408MHz}^{-1}$ ).

Pixel	K-band	Ka-band	Q-band	V-band	W-band	Pixel	K-band	Ka-band	Q-band	V-band	W-band
Free-Free Temperature C-C coefficients						Free-Free Polarization C-C coefficients					
1	-59.9 $\pm$ 23.9	-44.7 $\pm$ 25.1	-39 $\pm$ 24.4	-32 $\pm$ 29.6	-27.1 $\pm$ 33.4	1	-3 $\pm$ 5.8	0.8 $\pm$ 5.9	-5.4 $\pm$ 5.6	-0.7 $\pm$ 6.8	1.5 $\pm$ 8.3
2	67.2 $\pm$ 21.7	77.6 $\pm$ 22.8	80.9 $\pm$ 26.1	79 $\pm$ 27.6	62.8 $\pm$ 23.5	2	-2.6 $\pm$ 5.7	0.3 $\pm$ 5.7	1.7 $\pm$ 5.4	1.8 $\pm$ 6.6	7.9 $\pm$ 7.9
3	-44.5 $\pm$ 11.3	-40.6 $\pm$ 11.6	-42.1 $\pm$ 11.5	-41.1 $\pm$ 12.3	-33.3 $\pm$ 11.8	3	-10.6 $\pm$ 3.5	-0.3 $\pm$ 3.7	-0.1 $\pm$ 3.6	2.3 $\pm$ 4.5	1.6 $\pm$ 4.9
4	22.1 $\pm$ 3.5	12.8 $\pm$ 3.6	9.6 $\pm$ 4	5.7 $\pm$ 4.6	2.5 $\pm$ 4.8	4	-1.5 $\pm$ 1.2	-0.4 $\pm$ 1.3	-0.4 $\pm$ 1.2	0 $\pm$ 1.5	-1.9 $\pm$ 1.8
5	12.1 $\pm$ 10.1	8.4 $\pm$ 11.1	10 $\pm$ 10.5	4.9 $\pm$ 12.5	3.4 $\pm$ 11.3	5	-11.2 $\pm$ 2.8	-0.7 $\pm$ 2.8	-2.3 $\pm$ 2.8	-1.4 $\pm$ 3.4	4.5 $\pm$ 4.1
6	-8.1 $\pm$ 8.5	-10.4 $\pm$ 9.2	-10.2 $\pm$ 9.7	-11.6 $\pm$ 9.7	-9.2 $\pm$ 11.5	6	3.9 $\pm$ 2	0.2 $\pm$ 2	-0.3 $\pm$ 1.9	0.1 $\pm$ 2.3	0.8 $\pm$ 2.7
7	17.3 $\pm$ 7.3	10.4 $\pm$ 8.1	7.1 $\pm$ 8.4	5.7 $\pm$ 8.7	4.6 $\pm$ 10.3	7	-4.2 $\pm$ 1.6	-1.7 $\pm$ 1.7	-0.3 $\pm$ 1.5	0.2 $\pm$ 2	-0.7 $\pm$ 2.4
8	-10.3 $\pm$ 13.1	-10.7 $\pm$ 14.2	-10 $\pm$ 15.1	-9.9 $\pm$ 14.2	-5.6 $\pm$ 14.1	8	9 $\pm$ 3.5	1.4 $\pm$ 3.6	-0.4 $\pm$ 3.4	-0.5 $\pm$ 4.2	-0.5 $\pm$ 5
9	-3.3 $\pm$ 5.4	-7.4 $\pm$ 5.8	-8.1 $\pm$ 5.7	-9.9 $\pm$ 6.1	-8 $\pm$ 6.7	9	1.6 $\pm$ 1.6	0.4 $\pm$ 1.7	0.4 $\pm$ 1.6	0.7 $\pm$ 1.9	1.3 $\pm$ 2.3
10	19.6 $\pm$ 4.8	16.6 $\pm$ 5.1	15.3 $\pm$ 5.3	11.7 $\pm$ 5.9	8.7 $\pm$ 5.5	10	-0.3 $\pm$ 1.2	1.3 $\pm$ 1.2	0.1 $\pm$ 1.2	-0.4 $\pm$ 1.4	-1.3 $\pm$ 1.7
11	19.2 $\pm$ 3.3	16.8 $\pm$ 3.4	15.8 $\pm$ 3.9	13.7 $\pm$ 3.9	12.6 $\pm$ 3.4	11	0.5 $\pm$ 1.1	0.2 $\pm$ 1.1	1 $\pm$ 1.1	0.2 $\pm$ 1.4	-0.3 $\pm$ 1.6
12	6.4 $\pm$ 4.6	0.4 $\pm$ 5	-2.3 $\pm$ 5.4	-6.2 $\pm$ 4.9	-5.7 $\pm$ 5.5	12	0.8 $\pm$ 1.5	0 $\pm$ 1.5	0.7 $\pm$ 1.6	-0.8 $\pm$ 1.9	-1.9 $\pm$ 2.3
13	22.6 $\pm$ 2.1	14.3 $\pm$ 2.2	11.8 $\pm$ 2.5	7.8 $\pm$ 2.2	6.3 $\pm$ 2.5	13	-1.1 $\pm$ 0.8	0 $\pm$ 0.8	-0.5 $\pm$ 0.8	-0.7 $\pm$ 0.9	-0.3 $\pm$ 1.1
14	0 $\pm$ 3.7	-3.2 $\pm$ 3.8	-4 $\pm$ 4.3	-5.2 $\pm$ 4.2	-5.4 $\pm$ 4	14	-4.2 $\pm$ 0.8	-0.8 $\pm$ 0.8	-1.2 $\pm$ 0.8	-0.1 $\pm$ 0.9	-1.1 $\pm$ 1.1
15	15.2 $\pm$ 1.4	10.3 $\pm$ 1.5	8.6 $\pm$ 1.5	6.7 $\pm$ 1.5	5.7 $\pm$ 1.8	15	-1.5 $\pm$ 0.4	-0.4 $\pm$ 0.3	-0.2 $\pm$ 0.3	0 $\pm$ 0.4	0 $\pm$ 0.5
16	7.2 $\pm$ 1.7	3.1 $\pm$ 1.7	1.7 $\pm$ 1.8	-0.3 $\pm$ 1.8	-0.8 $\pm$ 2	16	0.5 $\pm$ 0.3	0.1 $\pm$ 0.3	0.4 $\pm$ 0.4	0 $\pm$ 0.4	-0.1 $\pm$ 0.5
17	-0.4 $\pm$ 1.9	-3.3 $\pm$ 2	-4.4 $\pm$ 2.2	-5.5 $\pm$ 2	-5 $\pm$ 2	17	-1 $\pm$ 0.5	0.3 $\pm$ 0.5	0.2 $\pm$ 0.5	0.1 $\pm$ 0.6	0.2 $\pm$ 0.7
18	3.1 $\pm$ 3.2	-1.1 $\pm$ 3.5	-3.2 $\pm$ 3.8	-3.6 $\pm$ 3.8	-3.6 $\pm$ 4	18	0.1 $\pm$ 0.9	0.7 $\pm$ 1	-0.3 $\pm$ 0.9	-0.2 $\pm$ 1.1	-0.2 $\pm$ 1.4
19	9.8 $\pm$ 0.6	5.6 $\pm$ 0.6	4 $\pm$ 0.7	2.2 $\pm$ 0.7	1.2 $\pm$ 0.6	19	0 $\pm$ 0.2	-0.1 $\pm$ 0.2	0 $\pm$ 0.2	0 $\pm$ 0.2	-0.2 $\pm$ 0.3
20	-1.8 $\pm$ 1.4	-2.6 $\pm$ 1.5	-3.4 $\pm$ 1.6	-3.9 $\pm$ 1.8	-3.9 $\pm$ 1.8	20	-0.6 $\pm$ 0.4	0.2 $\pm$ 0.5	0 $\pm$ 0.4	0 $\pm$ 0.5	0.1 $\pm$ 0.7
21	18.6 $\pm$ 4.2	6.7 $\pm$ 4.3	2.1 $\pm$ 5	1.2 $\pm$ 4.8	-2 $\pm$ 5.3	21	-2.1 $\pm$ 1.9	1.2 $\pm$ 2	-1.1 $\pm$ 1.9	-1 $\pm$ 2.3	-1.1 $\pm$ 2.9
22	11.7 $\pm$ 1.1	4.2 $\pm$ 1.2	1.7 $\pm$ 1.2	-0.5 $\pm$ 1.2	-1.2 $\pm$ 1.6	22	-0.8 $\pm$ 0.3	-0.2 $\pm$ 0.3	-0.3 $\pm$ 0.3	0 $\pm$ 0.4	0.4 $\pm$ 0.5
23	13.9 $\pm$ 1.8	8.9 $\pm$ 1.9	7.5 $\pm$ 2	5.4 $\pm$ 2.2	4.5 $\pm$ 2.6	23	0.2 $\pm$ 0.5	0 $\pm$ 0.5	-0.1 $\pm$ 0.5	-0.2 $\pm$ 0.6	-0.2 $\pm$ 0.8
24	7.5 $\pm$ 2.9	0.2 $\pm$ 3.2	-3 $\pm$ 3.1	-6 $\pm$ 3.4	-5.7 $\pm$ 3.3	24	-3.5 $\pm$ 0.8	-1.1 $\pm$ 0.8	-1 $\pm$ 0.8	-1 $\pm$ 1	-0.2 $\pm$ 1.2
25	9.8 $\pm$ 1.4	6.8 $\pm$ 1.4	5.9 $\pm$ 1.5	4.8 $\pm$ 1.5	3.5 $\pm$ 2	25	0.9 $\pm$ 0.5	0.5 $\pm$ 0.5	0.2 $\pm$ 0.5	0 $\pm$ 0.6	0 $\pm$ 0.7
26	10.3 $\pm$ 0.6	5.3 $\pm$ 0.6	3.6 $\pm$ 0.6	1.8 $\pm$ 0.7	0.9 $\pm$ 0.7	26	0.2 $\pm$ 0.2	0.1 $\pm$ 0.2	-0.1 $\pm$ 0.2	-0.1 $\pm$ 0.2	0.1 $\pm$ 0.2
27	3.6 $\pm$ 0.8	0 $\pm$ 0.8	-1.7 $\pm$ 0.9	-2.9 $\pm$ 0.9	-2.6 $\pm$ 0.9	27	-0.4 $\pm$ 0.2	-0.1 $\pm$ 0.2	0 $\pm$ 0.2	0 $\pm$ 0.3	-0.1 $\pm$ 0.3
28	-14.8 $\pm$ 4	-14.9 $\pm$ 4.1	-14.7 $\pm$ 4.8	-12.9 $\pm$ 4.9	-10.8 $\pm$ 5.3	28	2.6 $\pm$ 1.7	1.3 $\pm$ 1.7	-0.1 $\pm$ 1.6	-0.6 $\pm$ 2.1	0.4 $\pm$ 2.3
29	-1.1 $\pm$ 2.5	-1.9 $\pm$ 2.6	-2 $\pm$ 2.8	-2.6 $\pm$ 2.6	-3.6 $\pm$ 3.2	29	-3.6 $\pm$ 0.7	-1.8 $\pm$ 0.7	-1.4 $\pm$ 0.7	0.6 $\pm$ 0.9	0.2 $\pm$ 1
30	-1.6 $\pm$ 5.1	-0.7 $\pm$ 5.4	-0.5 $\pm$ 5.9	-2.2 $\pm$ 5.8	-3 $\pm$ 5.9	30	-4.1 $\pm$ 1.7	-0.4 $\pm$ 1.7	-1.7 $\pm$ 1.7	-0.5 $\pm$ 2.1	-0.5 $\pm$ 2.5
31	8.2 $\pm$ 1.1	2.6 $\pm$ 1.2	0.7 $\pm$ 1.3	-1 $\pm$ 1.3	-1.5 $\pm$ 1.4	31	-1.4 $\pm$ 0.3	0 $\pm$ 0.3	-0.2 $\pm$ 0.3	0.1 $\pm$ 0.3	-0.2 $\pm$ 0.4
32	12.2 $\pm$ 1.6	6.2 $\pm$ 1.7	3.7 $\pm$ 1.8	1.8 $\pm$ 1.9	0.9 $\pm$ 1.9	32	-0.5 $\pm$ 0.4	0.2 $\pm$ 0.4	-0.2 $\pm$ 0.4	0 $\pm$ 0.4	0.3 $\pm$ 0.5
33	7.7 $\pm$ 0.6	4.4 $\pm$ 0.7	3.3 $\pm$ 0.7	2 $\pm$ 0.7	1.2 $\pm$ 0.8	33	-0.3 $\pm$ 0.2	0.1 $\pm$ 0.2	0.1 $\pm$ 0.2	0.2 $\pm$ 0.3	0.3 $\pm$ 0.3
34	2.6 $\pm$ 0.5	0 $\pm$ 0.5	-1.2 $\pm$ 0.6	-2.2 $\pm$ 0.6	-2.4 $\pm$ 0.5	34	-0.1 $\pm$ 0.1	-0.1 $\pm$ 0.1	-0.1 $\pm$ 0.1	0 $\pm$ 0.2	0.2 $\pm$ 0.2
35	8 $\pm$ 0.4	4.6 $\pm$ 0.4	3.4 $\pm$ 0.5	1.9 $\pm$ 0.5	1.3 $\pm$ 0.5	35	-0.2 $\pm$ 0.1	-0.1 $\pm$ 0.1	-0.1 $\pm$ 0.1	0 $\pm$ 0.1	0 $\pm$ 0.1
36	-3.5 $\pm$ 1.6	-4.7 $\pm$ 1.7	-4.7 $\pm$ 1.7	-5 $\pm$ 1.7	-4.4 $\pm$ 2	36	-1 $\pm$ 0.4	-0.3 $\pm$ 0.4	-0.3 $\pm$ 0.3	-0.2 $\pm$ 0.4	0.5 $\pm$ 0.5
37	14.7 $\pm$ 9.4	17.7 $\pm$ 9.6	20.5 $\pm$ 10.3	16.5 $\pm$ 10.8	20.5 $\pm$ 10.9	37	-1 $\pm$ 3.4	0.9 $\pm$ 3.4	1.5 $\pm$ 3.3	0.2 $\pm$ 3.8	0.6 $\pm$ 4.8
38	14.7 $\pm$ 6.2	13.1 $\pm$ 6.7	11.3 $\pm$ 6.6	9.2 $\pm$ 8.1	6.9 $\pm$ 7.7	38	-7.3 $\pm$ 1.8	-4.1 $\pm$ 1.9	-0.8 $\pm$ 1.8	0.3 $\pm$ 2.2	-0.4 $\pm$ 2.7
39	21.1 $\pm$ 7.9	18.7 $\pm$ 8	20.3 $\pm$ 8.6	18.6 $\pm$ 9.8	11.7 $\pm$ 8.9	39	-7.1 $\pm$ 2.7	-1.3 $\pm$ 2.8	-2.5 $\pm$ 2.7	0.2 $\pm$ 3.3	-0.3 $\pm$ 4
40	14.1 $\pm$ 3.1	8.7 $\pm$ 3.3	5.8 $\pm$ 3.5	3.4 $\pm$ 3.2	4 $\pm$ 3.8	40	3.8 $\pm$ 1.1	0.3 $\pm$ 1.2	0.4 $\pm$ 1	0.3 $\pm$ 1.4	0.3 $\pm$ 1.5
41	4.3 $\pm$ 0.5	0.9 $\pm$ 0.6	-0.5 $\pm$ 0.6	-1.8 $\pm$ 0.6	-1.9 $\pm$ 0.7	41	0 $\pm$ 0.2	0 $\pm$ 0.2	0.1 $\pm$ 0.2	-0.1 $\pm$ 0.2	0 $\pm$ 0.3
42	3 $\pm$ 2.1	-0.2 $\pm$ 2.3	-1.2 $\pm$ 2.6	-2.5 $\pm$ 2.6	-2.6 $\pm$ 2.9	42	0.1 $\pm$ 0.5	0 $\pm$ 0.6	-0.2 $\pm$ 0.5	0 $\pm$ 0.6	0 $\pm$ 0.8
43	21.9 $\pm$ 3.3	16.2 $\pm$ 3.6	14.5 $\pm$ 3.7	11.8 $\pm$ 4.2	9.9 $\pm$ 4.1	43	-0.9 $\pm$ 1.2	0.5 $\pm$ 1.1	-1 $\pm$ 1	0 $\pm$ 1.3	0.2 $\pm$ 1.5
44	-8.4 $\pm$ 7.7	-9.6 $\pm$ 7.9	-9 $\pm$ 8.2	-8.6 $\pm$ 9.6	-9.3 $\pm$ 10.5	44	-7.3 $\pm$ 2.2	-2.6 $\pm$ 2.3	0.1 $\pm$ 2.2	0 $\pm$ 2.7	0.5 $\pm$ 3.2
45	-7.5 $\pm$ 16	-1.8 $\pm$ 16.5	2.8 $\pm$ 18.2	2.6 $\pm$ 19.3	-0.7 $\pm$ 20.4	45	5 $\pm$ 5.9	7.3 $\pm$ 6.1	1 $\pm$ 6	-0.7 $\pm$ 7.3	-1.2 $\pm$ 8.5
46	37.7 $\pm$ 11.4	35.7 $\pm$ 12.2	32.1 $\pm$ 13.2	29.7 $\pm$ 12.7	18.4 $\pm$ 13.2	46	1.2 $\pm$ 4.5	1.2 $\pm$ 4.8	-2.4 $\pm$ 4.6	-1.3 $\pm$ 5.6	7.2 $\pm$ 6.7
47	-17.9 $\pm$ 6.9	-24.7 $\pm$ 7.5	-26.5 $\pm$ 7.5	-28.3 $\pm$ 8.7	-24.7 $\pm$ 9.3	47	2.2 $\pm$ 1.6	1.6 $\pm$ 1.7	1.8 $\pm$ 1.5	-0.5 $\pm$ 1.8	1 $\pm$ 2.2
48	-25.9 $\pm$ 11.2	-27.7 $\pm$ 11.5	-28.5 $\pm$ 11.8	-25.4 $\pm$ 14.2	-23.5 $\pm$ 15.6	48	-0.4 $\pm$ 3.4	2.1 $\pm$ 3.6	-0.3 $\pm$ 3.3	-2.8 $\pm$ 4	2 $\pm$ 5

**Table A5.** Full fit temperature coefficients for free-free in all 48 pixel regions, with associated 1- $\sigma$  errors (in  $\mu K R^{-1}$ ).**Table A6.** Full fit coefficients for polarized free-free in all 48 pixel regions, with associated 1- $\sigma$  errors (in  $\mu K R^{-1}$ ).

